

The SRG/eROSITA All-Sky Survey

Constraints on AGN Feedback in Galaxy Groups

Y. E. Bahar^{1*}, E. Bulbul¹, V. Ghirardini¹, J. S. Sanders¹, X. Zhang¹, A. Liu¹, N. Clerc², E. Artis¹, F. Balzer¹, V. Biffi³, S. Bose⁴, J. Comparat¹, K. Dolag^{5,6}, C. Garrel¹, B. Hadzhiyska⁷, C. Hernández-Aguayo⁵, L. Hernquist⁸, M. Kluge¹, S. Krippendorf^{5,9}, A. Merloni¹, K. Nandra¹, R. Pakmor⁶, P. Popesso¹⁰, M. Ramos-Ceja¹, R. Seppi¹, V. Springel⁶, J. Weller^{1,5}, S. Zelmer¹

¹Max Planck Institute for Extraterrestrial Physics, Giessenbachstrasse 1, 85748 Garching, Germany

²IRAP, Université de Toulouse, CNRS, UPS, CNES, Toulouse, France

³INAF — Osservatorio Astronomico di Trieste, via Tiepolo 11, I-34143 Trieste, Italy

⁴Institute for Computational Cosmology, Department of Physics, Durham University, South Road, Durham, DH1 3LE, UK

⁵Universitäts-Sternwarte München, Fakultät für Physik, Ludwig-Maximilians-Universität, Scheinerstr. 1, 81679 München, Germany

⁶Max Planck Institute for Astrophysics, Karl Schwarzschild Str. 1, Garching, 85741, Germany

⁷Berkeley Center for Cosmological Physics, Department of Physics, University of California, Berkeley, CA 94720, USA

⁸Center for Astrophysics | Harvard & Smithsonian, 60 Garden Street, Cambridge, MA 02138, USA

⁹Arnold Sommerfeld Center for Theoretical Physics, Ludwig-Maximilians Universität, Theresienstr. 37, 80333 München, Germany

¹⁰European Southern Observatory, Karl Schwarzschildstrasse 2, 85748, Garching bei München, Germany

January 31, 2024

ABSTRACT

Context. Galaxy groups, lying between the galaxies and galaxy clusters in the mass spectrum of dark matter haloes, play a crucial role in the evolution and formation of the large-scale structure. Their shallower potential wells compared to clusters of galaxies make them excellent sources to constrain non-gravitational processes, such as feedback from the central active galactic nuclei (AGN).

Aims. We investigate the impact of feedback, particularly from AGN, on the entropy and characteristic temperature measurements of galaxy groups detected in the SRG/eROSITA's first All-Sky Survey (eRASS1) to shed light on the characteristics of the feedback mechanisms and help guide future AGN feedback implementations in numerical simulations.

Methods. We analyze the deeper eROSITA observations of 1178 galaxy groups detected in the eRASS1 Survey. We divide the sample into 271 subsamples based on their physical and statistical properties and extract average thermodynamic properties, including electron number density, temperature, and entropy, at three characteristic radii from cores to outskirts, along with the integrated temperature by jointly analyzing X-ray images and spectra following a Bayesian approach.

Results. We present the tightest constraints with unprecedented statistical precision on the impact of AGN feedback through our average entropy and characteristic temperature measurements of the largest group sample used in X-ray studies, incorporating major systematics in our analysis. We find that entropy shows an increasing trend with temperature in the form of a power-law-like relation at the higher intra-group medium (IGrM) temperatures, while for the low mass groups with cooler ($T < 1.44$ keV) IGrM temperatures, a slight flattening is observed on the average entropy. Overall, the observed entropy measurements agree well with the earlier measurements in the literature. Additionally, the comparisons with the state-of-the-art cosmological hydrodynamic simulations (MillenniumTNG, Magneticum, OWL simulations) after the applications of the selection function calibrated for our galaxy groups reveal that observed entropy profiles in the cores are below the predictions of simulations. At the mid-region, the entropy measurements agree well with the Magneticum simulations, whereas the predictions of MillenniumTNG and OWL simulations fall below observations. At the outskirts, the overall agreement between the observations and simulations improves, with Magneticum simulations reproducing the observations the best.

Conclusions. These measurements will pave the way for achieving more realistic AGN feedback implementations in numerical simulations. The future eROSITA Surveys will enable the extension of the entropy measurements in even cooler IGrM temperatures below 0.5 keV, allowing the test of the AGN feedback models in this regime.

Key words. Galaxies: groups: general–Galaxies: clusters: general–Galaxies: clusters: intracluster medium–X-rays: galaxies: clusters

1. Introduction

In the current understanding of the "bottom-up" structure formation of the Universe in the standard Λ CDM cosmology, small overdensities collapse first, overcoming the cosmological expansion, merging to form larger haloes (Springel 2005). In this

scenario, the gas encapsulated in dark matter haloes forms the first stars and galaxies as it cools and condenses. The effects of tidal forces, mergers, and interactions in their surroundings regulate the galaxy formation and evolution process. The majority of galaxies in the Universe are found in dense environments as galaxy groups and include a large fraction of the universal baryon budget (Mulchaey 2000). The interaction between

* e-mail: ebahar@mpe.mpg.de

galaxies and the intra-group medium (IGrM; the gas encapsulated within the galaxy groups) plays a crucial role in shaping the properties and evolution of galaxies. For instance, the feedback from supernovae, star formation, and central supermassive black holes impacts the evolution of galaxies within the galaxy groups.

Although there is no clear definition of galaxy groups, dark matter haloes with less than 50 galaxies and/or masses between $5 \times 10^{12} - 10^{14} M_{\odot}$ are classified as galaxy groups (Crain et al. 2009) in the literature. In addition to their member galaxies, galaxy groups contain diffuse baryonic matter in the form of hot plasma with temperatures (T^1) ranging from 0.1–2 keV, all encapsulated by the potential well provided by dark matter. Groups are further categorized as poor/loose groups, compact groups, and fossil groups depending on their optical properties (Hickson 1997; Mulchaey & Zabludoff 1998; Mulchaey 2000; Voevodkin et al. 2010).

Despite the abundance of galaxy groups and the essential role they play in the assembly process of dark matter haloes in the Universe (Crain et al. 2009), their detection has been challenging due to their low richness, faint X-ray signal, and shallow potential wells. A variety of methods have been employed to search for galaxy groups. In the optical domain, clustering and friends-of-friends (FoF) algorithms are used to catalog groups in spectroscopic or photometric galaxy redshift surveys (e.g., Hickson 1982; Robotham et al. 2011; Tempel et al. 2017; Gozaliasl et al. 2022). However, due to their relatively low richnesses, group catalogs compiled using optical observations may suffer from large contamination fractions due to random superposition of galaxies along the line-of-sight, otherwise known as projection effects (see Costanzi et al. 2019; Grandis et al. 2021; Myles et al. 2021). On the other hand, in the X-ray domain, the emission from IGrM makes them appear as extended sources in the X-ray sky, where they typically exhibit rapidly increasing X-ray emission profiles from the outskirts of the system to the center. Because of their characteristic surface brightness profiles, if their emission is above the background level, they can be easily identified and do not suffer significantly from projection effects. Aside from being a reliable tool for detecting groups, X-ray observations also enable the measurement of the physical properties of the hot ionized IGrM through imaging and spectral analysis.

The effects of the non-thermal astrophysical phenomena governing galaxy formation are easier to study using galaxy groups compared to clusters as the input energy associated with these phenomena is comparable to the binding energies of groups (Balogh et al. 2001). For investigating the non-thermal phenomena, entropy ($S = T/n_e^{2/3}$) measurements of IGrM are often used, which retains a historical record of the thermodynamic state of the gas and reflects the changes in the cooling and heating processes in galaxy groups (Voit et al. 2005; Pratt et al. 2010). For example, OverWhelmingly Large Simulations (OWLS, Schaye et al. 2010; McCarthy et al. 2010) showed that the outflows from the central active galactic nuclei (AGN) elevate the entropy of the IGrM by mechanically expelling low-entropy gas instead of directly heating it. This process mitigates rapid cooling and prevents excessive star formation (Bryan 2000; Balogh et al. 2001). On the other hand, the feedback generated by supernova-driven winds associated with galaxies can also increase the entropy of the IGrM through direct heating (see Eckert et al. 2021, for a review).

¹ Throughout this paper, we use the notation T to represent $k_B T$ and express temperature measurements in the units of keV.

Entropy of IGrM can be measured using X-ray observations, where the electron density and temperature measurements can be made using the imaging and spectroscopic capabilities of X-ray telescopes, such as SRG/eROSITA, XMM-Newton, and Chandra. Ponman et al. (1999) measured the entropy of 25 bright galaxy clusters and groups at a radius of $0.1 r_{\text{virial}}^2$ using ROSAT and GINGA observations and reported that the entropy measurements at the core lay above the expected power-law relation with temperature for the first time. Subsequently, Lloyd-Davies et al. (2000), Finoguenov et al. (2002) and Ponman et al. (2003) measured the entropy profiles of galaxy clusters and groups using ROSAT and ASCA observations that provided the first hint that in galaxy groups, the excess entropy is not limited only to the core but can also be prominent at larger radii. Voit et al. (2005) formulated a baseline entropy profile that can be used for evaluating the impact of non-gravitational processes for galaxy clusters and groups using four sets of simulations that only include gravitational processes. Using X-ray instruments with a higher spatial and spectral resolution, such as XMM-Newton and Chandra, significantly improved our understanding of the excess entropy in galaxy groups by accurately measuring their entropy profiles. Johnson et al. (2009) investigated entropy profiles of galaxy groups by analyzing XMM-Newton observations of 28 nearby galaxy groups from the Two-Dimensional XMM-Newton Group Survey. They divided their sample into two subsamples, cool core, and non-cool core, based on the temperature gradient at the core of their groups and found that the entropy profiles of the groups in their non-cool core sample exhibit less scatter compared to entropy profiles of their cool core sample. Around the same time, Sun et al. (2009, S09 hereafter) conducted a comprehensive study on the thermodynamic gas properties of 43 nearby galaxy groups using the archival Chandra observations where they constrained the temperature, electron density, and metallicity profiles of 23 groups out to r_{500c}^3 accurately, thanks to the outstanding imaging capabilities of Chandra and the relatively deep archival observations of some systems in their sample. Furthermore, they compared their entropy profiles with the baseline entropy profile of Voit et al. (2005) and found that even though the entropy excess reduces as a function of the radius, it remains significant out to r_{500c} . Subsequently, the detailed analysis of the outskirts of RX J1159+5531, UGC 03957, and Virgo using Suzaku observations revealed that the entropy excess can go beyond r_{500c} (Humphrey et al. 2012; Thölken et al. 2016; Simionescu et al. 2017). More recently, Panagoulia et al. (2014) analyzed 66 galaxy groups from the NORAS and REFLEX samples to investigate the properties of IGrM at the core and found that entropy profiles of galaxy groups at the core follow a power-law relation and do not exhibit any entropy floor.

Previous studies in the literature on the thermodynamic properties of galaxy groups have been conducted using relatively small (less than a hundred) and highly incomplete samples that lack well-defined selection functions. eROSITA opens a new window for galaxy group studies by providing the largest pure X-ray-selected sample with a well-defined selection function crucial for achieving robust conclusions that reflect the physical properties of the galaxy group well at the population level. Furthermore, the superb soft X-ray band sensitivity and the scanning observing strategy of eROSITA make it an excellent instrument

² r_{virial} is defined as the radius within which a system obeys the virial theorem.

³ r_{500c} is defined as the radius within which the density of a system is 500 times the critical density of the Universe at the redshift of the system.

for investigating the physical properties of the hot gas in galaxy groups, given that the emission of IGrM peaks at the soft X-ray band and the brightest galaxy groups above the detection capabilities of the current instruments are at low redshift and well extended.

In this work, we examine the effect of the feedback on the thermodynamics of galaxy groups detected by eROSITA in its first All-Sky Survey. We accomplish this by performing joint imaging and spectral analysis on the eRASS:4 (the four eROSITA consecutive All-Sky Surveys stacked together) observations of the galaxy groups in our sample. The extended ROentgen Survey with an Imaging Telescope Array (eROSITA), the soft X-ray telescope on board the Spectrum-Roentgen-Gamma (SRG) mission (Sunyaev et al. 2021), was launched on July 13, 2019 (Predehl et al. 2021). The first All-Sky Survey with eROSITA was successfully executed on June 11, 2020, after 184 days of operations. In this first All-Sky Survey (eRASS1), eROSITA detected a total of 12247 optically confirmed galaxy groups and clusters spanning the redshift range $0.003 < z < 1.32$ with a sample purity level of 86% in the Western Galactic half of the survey ($359.9442 \text{ deg} > l > 179.9442 \text{ deg}$), where the data rights belong to the German eROSITA consortium (Merloni et al. 2024; Bulbul et al. submitted; Kluge et al. submitted).

In this paper, we combine the imaging and spectroscopic information of 1178 eROSITA-detected galaxy groups and obtain average entropy measurements at $0.15r_{500c}$, r_{2500c} and r_{500c} to investigate the effects of AGN feedback and compare our findings with the state-of-the-art numerical simulations from MillenniumTNG (Hernández-Aguayo et al. 2023; Pakmor et al. 2023), Magneticum (Hirschmann et al. 2014), and OverWhelmingly Large simulations (Schaye et al. 2010; McCarthy et al. 2010). The findings represent the first study of a comprehensive group sample with a well-defined selection function. This paper is organized as follows: In Sect. 2, we describe the construction of the galaxy groups sample from the primary eRASS1 sample, and in Sect. 3, we describe the X-ray data reduction and the analysis of the groups. In Sect. 4, we provide a discussion of major systematics and the details of the quantification and incorporation of them in our results, and in Sect. 5, we provide our final results on the entropy measurements of the sample and comparisons with the previous measurements. In Sect. 6, we provide a comparison between our measurements and the predictions of the state-of-the-art simulations. Lastly, we provide a summary of our findings and list our conclusions in Sect. 7. Throughout this paper, we adopt a flat Λ CDM cosmology using the Planck Collaboration et al. (2016) results, namely $\Omega_m = 0.3089$, $\sigma_8 = 0.8147$, and $H_0 = 67.74 \text{ km s}^{-1} \text{ Mpc}^{-1}$. Quoted error bars correspond to a $1-\sigma$ confidence level unless noted otherwise.

2. Sample of Galaxy Groups

This work utilizes a subsample of the X-ray-selected, optically identified primary eRASS1 galaxy cluster and group sample detected in the Western Galactic hemisphere of the first eROSITA All-Sky Survey (Bulbul et al. submitted; Kluge et al. submitted). Below, we briefly describe the detection of galaxy clusters and groups in eRASS1 observations and a brief summary of the optical and X-ray cleaning performed in Bulbul et al. (submitted). Subsequently, we provide the details of the additional selection and cleaning applied to the eRASS1 galaxy clusters and groups catalog.

The X-ray emitting celestial objects in the eRASS1 master X-ray catalog (Merloni et al. 2024) are detected using the eROSITA source detection pipeline, which is part of the

eROSITA Science Analysis Software System (eSASS, Brunner et al. 2022). The pipeline locates detection candidates and calculates detection and extent likelihood (\mathcal{L}_{det} and \mathcal{L}_{ext}) parameters by comparing the spatial distribution and the abundance of the photons around the candidate with the local background. To construct the primary galaxy groups and clusters sample (Bulbul et al. submitted), a $\mathcal{L}_{\text{ext}} > 3$ cut is applied to increase the completeness of the galaxy groups and clusters sample (see Bulbul et al. 2022, for the motivation). The DESI Legacy Survey DR9 and DR10 datasets are used in the optical identification processes by the eROMaPPER pipeline, which is based on the matched-filter red-sequence algorithm from redMaPPER (Rykoff et al. 2014, 2016) tailored and optimized for the identification of eROSITA extended sources (Ider Chitham et al. 2020; Kluge et al. submitted). If available, spectroscopic redshifts (z_{spec}) are prioritized over photometric redshift (z_{λ}) by the eROMaPPER pipeline (see Kluge et al. submitted, for further details). In this primary sample, 12 705 extended sources in the redshift range of 0.01 to 1.35 are identified as galaxy clusters or groups with a contamination fraction of 14% (Bulbul et al. submitted; Kluge et al. submitted).

To construct a final clean and secure galaxy group sample, we apply further cuts based on the X-ray and optical properties of the primary sample. While the literature lacks a precise definition for galaxy groups, we classify an object as a group if its mass ranges between $5 \times 10^{12} < M_{500c} < 10^{14} M_{\odot}$. The upper end of our group definition ($10^{14} M_{\odot}$) corresponds to a plasma temperature of $T \sim 2 \text{ keV}$ and is commonly used in previous X-ray studies for distinguishing galaxy clusters from galaxy groups (Lovisari et al. 2021). For incorporating this mass criterion, we use the M_{500c} estimates obtained in Sect. 3.3 using a Bayesian X-ray observable estimation framework that jointly estimates the soft-band (0.5–2 keV) X-ray luminosity (L_X), temperature (T) and the mass (M_{500c}) of galaxy clusters and groups from their count-rate profiles (see Sect. 3.3 for the details of our $L_X - T - M_{500c}$ estimation). After applying a mass cut of $M_{500c} < 10^{14} M_{\odot}$, we select 2526 galaxy group candidates with a median redshift of 0.11.

To further reduce the contamination, we apply other cleaning methods using the deeper eRASS:4 data. Contaminants in the $\mathcal{L}_{\text{ext}} > 3$ sample of the eRASS1 clusters and groups catalog can be classified into two categories: misclassified sources (mostly AGN) and spurious sources. Given that our preliminary sample has a median redshift of 0.11, the "real" galaxy groups in our sample are expected to be relatively well extended in the sky, whereas misclassified point sources, by definition, should have a low extent. We make use of this fact and conservatively remove 841 objects that have $\text{EXT} < 20 \text{ arcsec}$ and $\mathcal{L}_{\text{ext}} < 5.5$. These cuts remove most point sources, leaving 1685 group candidates in the sample.

Once the misclassified point sources are removed, spurious sources are left to be cleaned from our group sample. We use the count measurements in the 0.3 – 1.8 keV band (see Appendix A for the details on the choice of the energy band) obtained from eRASS:4 observations as described in Sect. 3.2 to clean the spurious sources. We first apply an X-ray count cut of 10. This cut removes 423 objects from our group candidates. Furthermore, we remove 10 more sources from the remaining sample with count measurements 1σ consistent with the background level. This procedure removes most of the spurious sources since one would expect the galaxy groups to be more prominent and bright as the survey gets deeper. On the other hand, the spurious sources are expected to have low counts and be consistent with the background level since they are mostly due to background fluctuations or superpositions of undetected AGN in the eRASS1 ob-

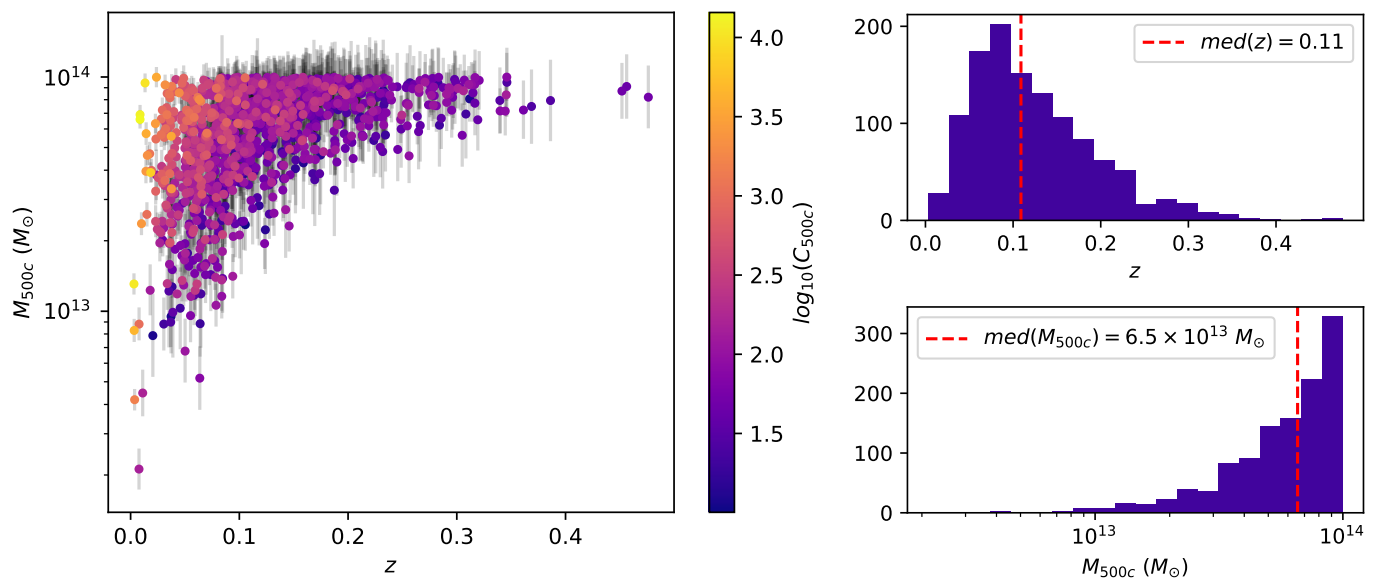


Fig. 1: *Left*: The mass and redshift distributions of the galaxy group sample used in this work consist of 1178 objects where colors of the data points represent the eROSITA counts of the groups in soft X-ray band (0.3 – 1.8 keV) *Right*: Mass and redshift histograms of the group sample where the median redshift (z) is 0.11 and median mass (M_{500c}) is $6.5 \times 10^{13} M_{\odot}$.

servations. Applying these cuts, we remove a large fraction of contaminants in our sample and obtain a highly pure sample with 1252 galaxy groups.

One of the major benefits of the strict cleaning procedure described above is its applicability to simulations. Our cleaning procedure relies upon the detection pipeline outputs (e.g., \mathcal{L}_{ext} and EXT) and therefore the selection process is fully reproducible in the simulations of the eRASS1 digital twin (Comparat et al. 2020; Seppi et al. 2022). This allows us to construct a robust selection function for our sample using the eROSITA’s digital twin simulations. We further note that the cleaning applied in this work to remove spurious sources has no impact on the selection function⁴.

Following the cleaning procedure, we visually inspect the groups that are centrally peaked ($r_c < 32$ arcsec)⁵ and have low extent likelihoods ($\mathcal{L}_{ext} < 10$) using the eRASS:4 and the Legacy Survey data. As a result of the visual inspection, we further flagged and removed 74 falsely classified point sources from our sample. These objects make a small fraction of our clean sample (6%); therefore, their removal has a negligible impact on the selection function, especially compared to the systematic uncertainties of X-ray simulations at group scales used to construct the selection function. The final sample, consisting of 1178 galaxy groups, has a median redshift of 0.11 and a median mass (M_{500c}) of $6.3 \times 10^{13} M_{\odot}$. The Redshift and mass distributions of the final sample can be seen in the right panel of Fig. 1. Moreover, the 2D projected distribution of these groups in the eROSITA sky is shown in Fig. 2. We note that some of the "cleaning" procedures described above (e.g., the EXT and \mathcal{L}_{ext} cuts) not only clean spurious sources but also unavoidably remove some of the faint real groups from the sample according to the expected purity of

⁴ The selection function, $P(I|O)$, can be seen as the ratio of the number of the detected "real" objects to the number of all the "real" objects within the infinitesimal observable parameter space of $(O, O + dO)$. Removal of confirmed spurious sources does not change this ratio and, therefore, has no impact on $P(I|O)$.

⁵ See Eq. 1 for the definition of r_c and Sect. 3.2 for the details of the imaging analysis.

the eRASS1 cluster sample in the cost of achieving a more secure groups sample. Nevertheless, the resulting extra selection is taken into account in our analysis by incorporating a selection function built for our final sample. After the cleaning procedure described above, our sample ended up having three objects with mass estimates slightly below the lower bound of our group mass definition ($5 \times 10^{12} M_{\odot} < M_{500c} < 10^{14} M_{\odot}$). We eventually decided to keep them in our group sample since the removal of three objects has little to no impact on our final results, and their "true" masses can well be within our group mass definition due to the intrinsic scatter of the $L_X - M_{500c}$ relation.

The final galaxy group sample described above is obtained to construct a well-defined selection function using eROSITA’s twin simulations. A good handle on selection effects is key for achieving universal conclusions about the properties and the governing physics of studies of groups. The deeper eRASS:4 observations of an unprecedented number of galaxy groups we use in this work are particularly well-suited for studying the baryonic physics in galaxy groups because of the higher statistics allowed by the deeper survey data and large field-of-view necessary to measure the X-ray properties out to large radii. In the next section, we present our eRASS:4 analysis of the galaxy groups in the sample.

3. Data Analysis

3.1. X-ray Data Reduction and Analysis

Taking advantage of the higher signal-to-noise deeper survey observation, we use the eRASS:4 observations of the eRASS1 selected galaxy groups with the processing version 020 (briefly described in Appendix C of Merloni et al. 2024), that is an updated version of 010 processing used for the first data release (DR1). The main updates on the 020 version (internal catalog version 221031) are the improved boresight correction, low-energy detector noise suppression, improved subpixel resolution, and updated pattern and energy tasks. We further reduce the calibrate event files using the using the eROISTA Science Analysis Soft-

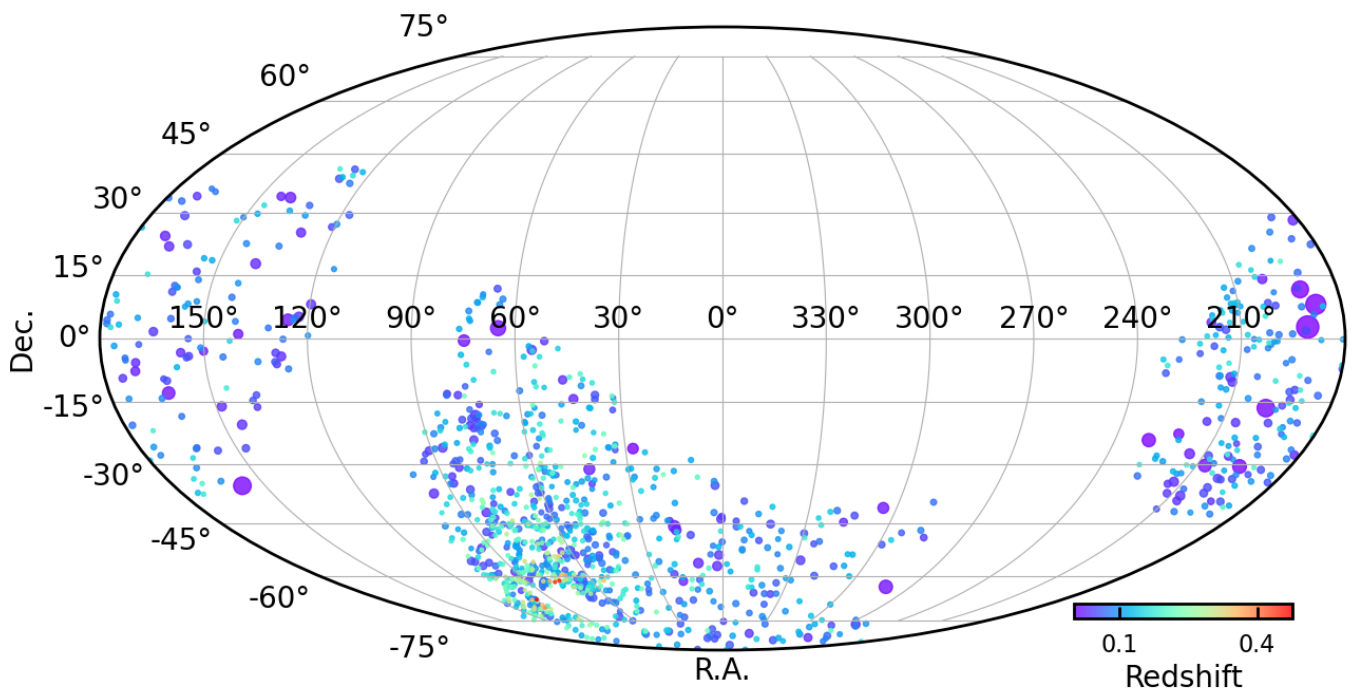


Fig. 2: The projected locations of the 1178 galaxy groups in the primary catalog in the eROSITA and Legacy Survey DR9N and DR10 13,116 deg² common footprints are shown. The redshift confirmed by the follow-up algorithm eROMAPPer is color-coded (Kluge et al. submitted), while the sizes of the detections are scaled with the angular sizes (r_{500c}) of the groups (see Sect. 3.3 for the r_{500c} estimation procedure). The inhomogeneity of the source density in this figure is due to the exposure variation across the eROSITA-DE X-ray sky (see Fig. 2 in Bulbul et al. submitted).

ware System (eSASS, Brunner et al. 2022)⁶ with the version id eSASSusers_211214 that is the same version used for Bulbul et al. (submitted) and Merloni et al. (2024) for DR1. Time variable (solar incident angle dependent) optical light contamination (light leak) is observed in the data from the telescope modules (TMs) 5 and 7, which has a large impact on the calibration of the low-energy band of the spectrum (see Predehl et al. 2021; Coutinho et al. 2022; Merloni et al. 2024, for further details). In this work, we analyze the hot gas properties of galaxy groups whose emission peaks at the soft X-ray band that suffers from the contamination; therefore, we follow a conservative approach and only use the data from TMs 1, 2, 3, 4, and 6, removing the TM5 and 7, suffering from contamination from the optical light leak. Furthermore, we obtain a clean event list by applying the standard flag `0xE000F000` to select all the possible patterns (singles, doubles, triples, and quads) and run the `flaregti` eSASS task to have flare filtered good-time-intervals.

3.2. Imaging analysis

For the imaging analysis, we use an energy band of 0.3–1.8 keV to maximize the signal-to-noise ratio (SNR) for a soft X-ray emitting source such as groups (see Appendix A for the details of this optimization scheme). We extract images, vignetted and non-vignetted exposure maps in this band centered around each group in the catalog using the `evttool` and `expmap` tasks in eSASS with a standard eROSITA pixel size of 4 arcsec and the `FLAREGTI` option. For the extraction region, we use an image size of $\sim 8r_{500c,eSASS} \times 8r_{500c,eSASS}$ that covers well the region

from the source center beyond the Virial radius for the local background measurements. The radius, $r_{500c,eSASS}$, is estimated using the flux reported in column `ML_FLUX_1` of the eRASS1 X-ray catalog (Merloni et al. 2024) and an $L_X - M_{500c}$ relation of the eROSITA Depth Final Equatorial Survey (eFEDS) clusters and groups (Bahar et al. 2022; Chiu et al. 2022). These estimates are only used to determine the image size that has a negligible impact on the results. After generating X-ray images and exposure maps, we use the eRASS:4 point source catalog in the 0.2–2.3 keV band to mask or co-fit the point sources in the field of view (FOV) in the rest of the imaging analysis. Following the same procedure in our eFEDS analysis (Ghirardini et al. 2021; Liu et al. 2022; Bahar et al. 2022), we mask the faint point sources with `ML_RATE_1 < 0.1` cts/s out to the radii where their emission becomes consistent with the background. On the other hand, we co-fit bright point sources (`ML_RATE_1 > 0.1` cts/s) in the surface brightness analysis. In addition to the bright point sources, we also model and co-fit the closest extended sources to the central galaxy group to clean the image from contaminating X-ray emission. The remaining ones in the field are conservatively masked out to their $2r_{500c,eSASS}$. Example eROSITA images of a bright nearby group (1eRASS J024933.9-311126) and a group at the median redshift of our group sample (1eRASS J045547.0-572404) are shown in Fig. 3.

Following a forward modeling approach, we fit the X-ray images using a Bayesian fitting pipeline to deproject the surface brightness emission. We assume a Poisson likelihood for the X-ray counts and sample the likelihood using the `emcee` package (Foreman-Mackey et al. 2013) that employs the Goodman & Weare (2010) Affine Invariant Markov chain Monte Carlo (MCMC) technique. The fit is performed to account for the

⁶ <https://erosita.mpe.mpg.de/dr1/eSASS4DR1/>

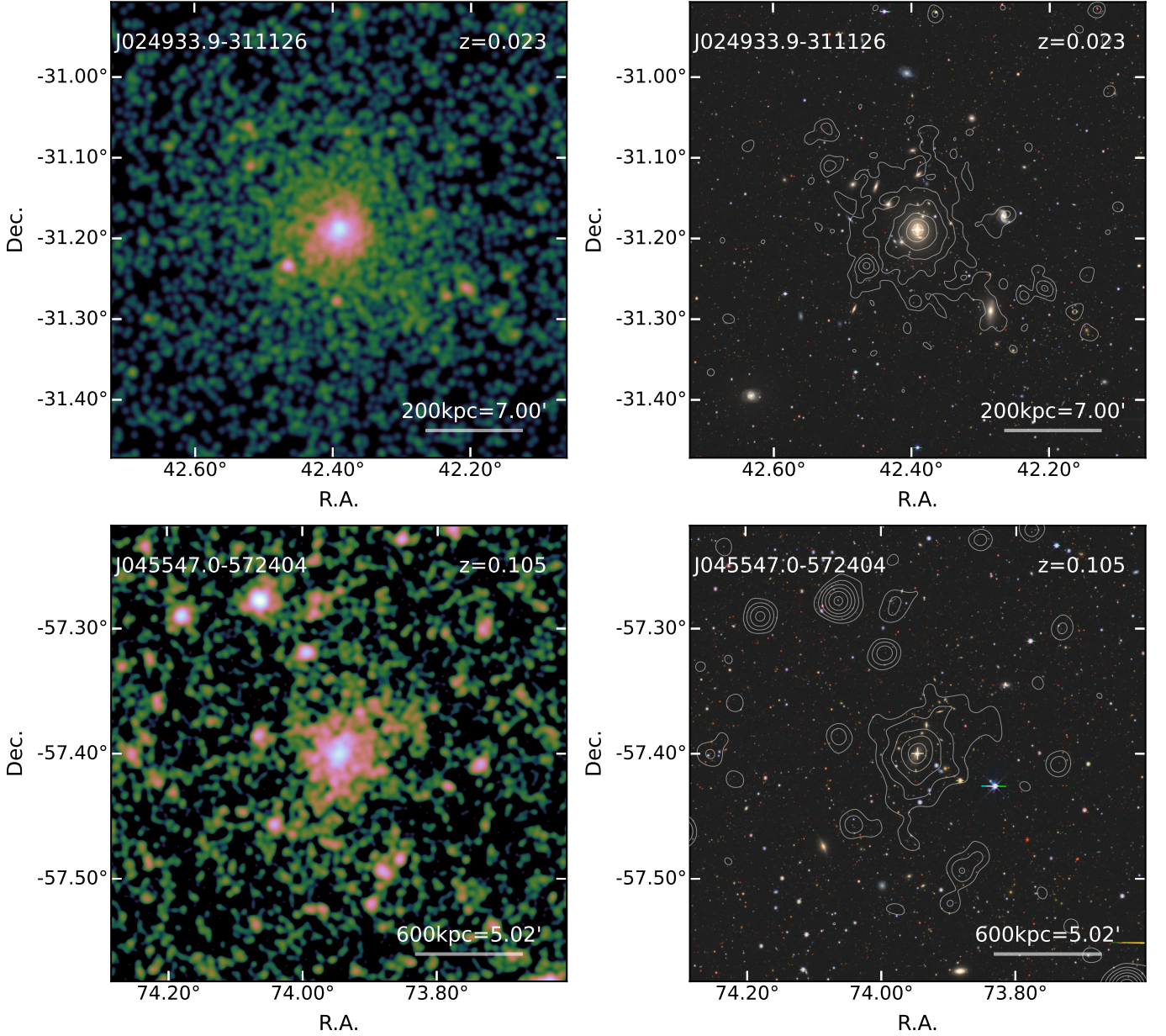


Fig. 3: *Left*: eRASS:4 soft band 0.3–1.8 keV images of two bright groups (1eRASS J024933.9-311126 and 1eRASS J045547.0-572404) at redshifts 0.023 and 0.105. *Right*: The Legacy Survey DR10 images of the same groups with the eRASS:4 X-ray contours overlaid.

cross-talk between the emission from the nearby co-fitted extended and point sources. For extended sources, we model emissivity using a modified [Vikhlinin et al. \(2006\)](#) profile:

$$\Lambda_{\text{ep}}(T, Z) n_{\text{e}}^2(r) = n_0^2 \left(\frac{r}{r_c} \right)^{-\alpha} \left(1 + \left(\frac{r}{r_s} \right)^2 \right)^{-3\beta + \alpha/2} \left(1 + \left(\frac{r}{r_s} \right)^3 \right)^{-\epsilon/3}, \quad (1)$$

where $\Lambda_{\text{ep}}(T, Z)$ is the band-averaged cooling function, Z is the metallicity and n_0 , r_c , r_s , α , β , ϵ are the free parameters of the electron density profile, normalization, core radius, scale radius, and the power law exponents, respectively. These parameters are allowed to vary in the fits. At each MCMC step, the profile is projected along the line of sight following the equation:

$$S_X = \frac{1}{4\pi(1+z)^4} \int n_e n_p \Lambda_{\text{ep}}(T, Z) dl, \quad (2)$$

where the number density of protons (n_p) are related to the number density of electrons (n_e) via $n_p = n_e/1.2$ ([Bulbul et al. 2010](#)). Then, the projected count rate is convolved with the eROSITA point spread function (PSF), multiplied with the exposure map, and compared with the masked X-ray image. In addition to the electron density profile parameters, two additional parameters are left free for the central position of the groups, which adds up to eight free parameters for every extended source modeled in the image. For the bright point sources, we only allow the normalization of their profile to vary while keeping the centroids fixed due to the high positional accuracy of eROSITA ([Brunner](#)

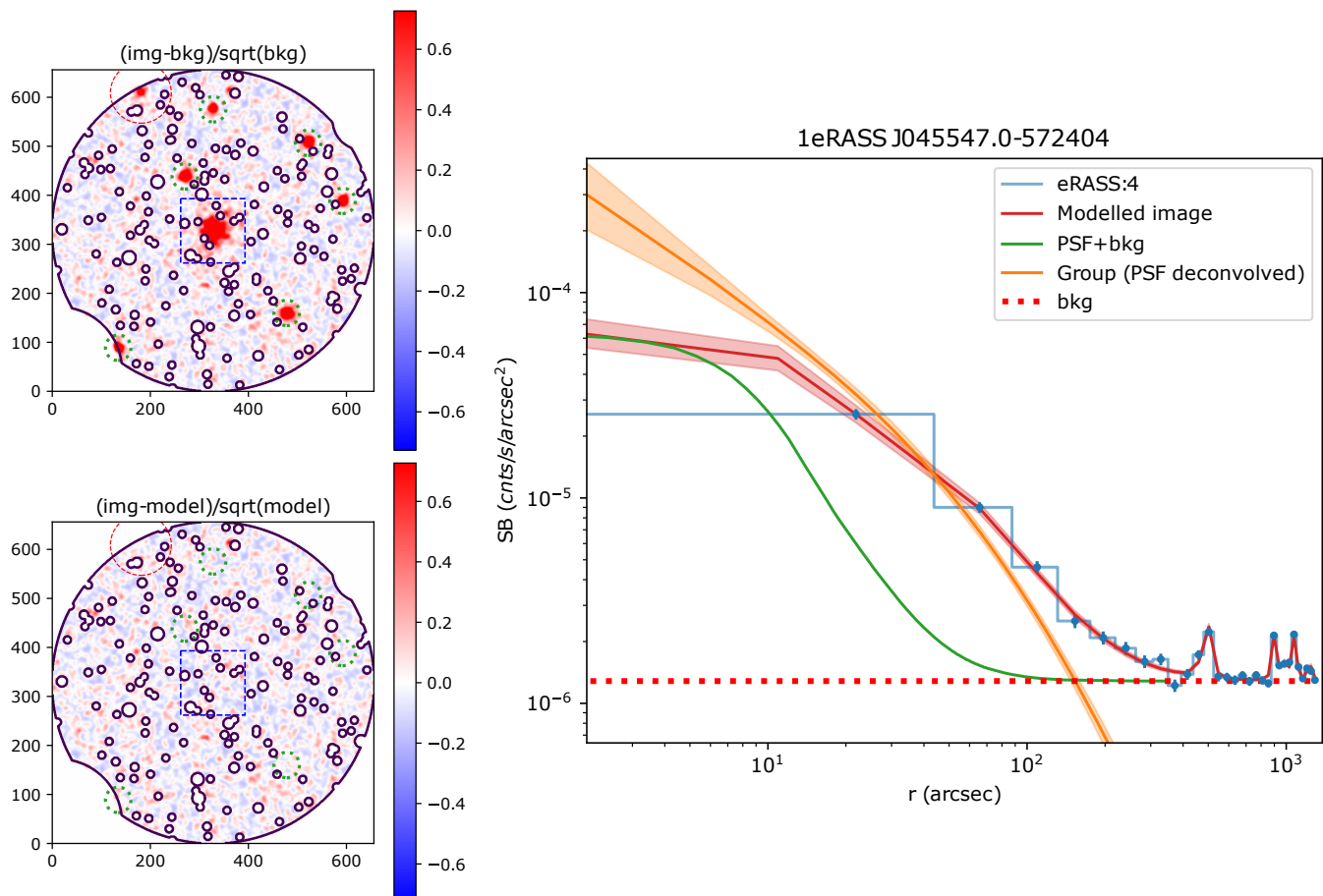


Fig. 4: An example of the eROSITA imaging analysis for the group 1eRASS J045547.0-572404. *Left*: The residual image of the group before and after subtracting the co-fit extended sources and point sources in the field. Nearby co-fit clusters and groups are shown with red circles, co-fit nearby bright AGN are shown with green circles, and the fitted galaxy group is shown with a blue rectangle. The smooth noise level indicates that the contaminant emission is modeled properly in the analysis. *Right*: Surface brightness profile of the same group. The observed surface brightness profile of the image is plotted in blue, the best-fit model of the image is plotted in red, the PSF profile over the measured background is plotted in green, the PSF deconvolved surface brightness profile of the galaxy group is plotted in orange, and the measured background level is shown with a dashed red line.

et al. 2022; Merloni et al. 2024). Lastly, for each image, the background count rates are assumed to be constant across the image, and two more parameters are allowed to be free for the vignettted and unvignettted backgrounds.

As an output of this fitting procedure, we obtain the best-fit de-projected emissivity profiles ($\Lambda_{\text{ep}}(T, Z) n_{\text{e}}^2(r)$), count-rate profiles, and the associated uncertainties that include the cross-talk between the co-fitted nearby extended and point sources. We show the performance of our pipeline in Fig. 4 for a bright group (1eRASS J045547.0-572404, the second group in Fig. 3) with the images before and after subtracting the emission from the modeled extended and point sources on the left. It is clear from the bottom left figure that after the removal of the modeled profiles, the image is free from any X-ray source, and only noise remains. The surface brightness profile of the observed field (in blue) and the best-fit model (in red) are shown on the right panel of the same figure. The PSF convolved best-fit surface brightness model represents the eROSITA data well. The peaked emission at large radii (at 500 and 1000 arcsec) shows the contribution of the modeled point sources to the overall emission, which are successfully modeled and removed from the total source model.

3.3. Estimation of X-ray Observables

The shallow nature of the eROSITA survey only allows the measurement of the physical properties of a few nearby bright galaxy groups. The eRASS1 group sample should be binned into smaller samples to achieve sufficient signal-to-noise for reliably constraining the physical properties of the faint galaxy groups through joint spectral analysis (see Sect. 3.4). For an optimal binning scheme, a low-scatter temperature estimator should be used such that groups with similar temperatures can be binned together. Moreover, mass estimates of the galaxy groups are needed to extract spectra within a physically motivated scale radii (r_{500c}). For these purposes, we use $L_X - M_{500c}$ and $L_X - T$ scaling relations and calculate the soft-band (0.5 – 2 keV) X-ray luminosity (L_X), temperature (T), and mass (M_{500c}) estimates of the galaxy clusters and groups from the count-rate profiles measured in Sect. 3.2. For a self-consistent treatment of the eROSITA groups, we employ the $L_X - M_{500c}$ and $L_X - T$ relations calibrated using the eFEDS observations (Chiu et al. 2022; Bahar et al. 2022).

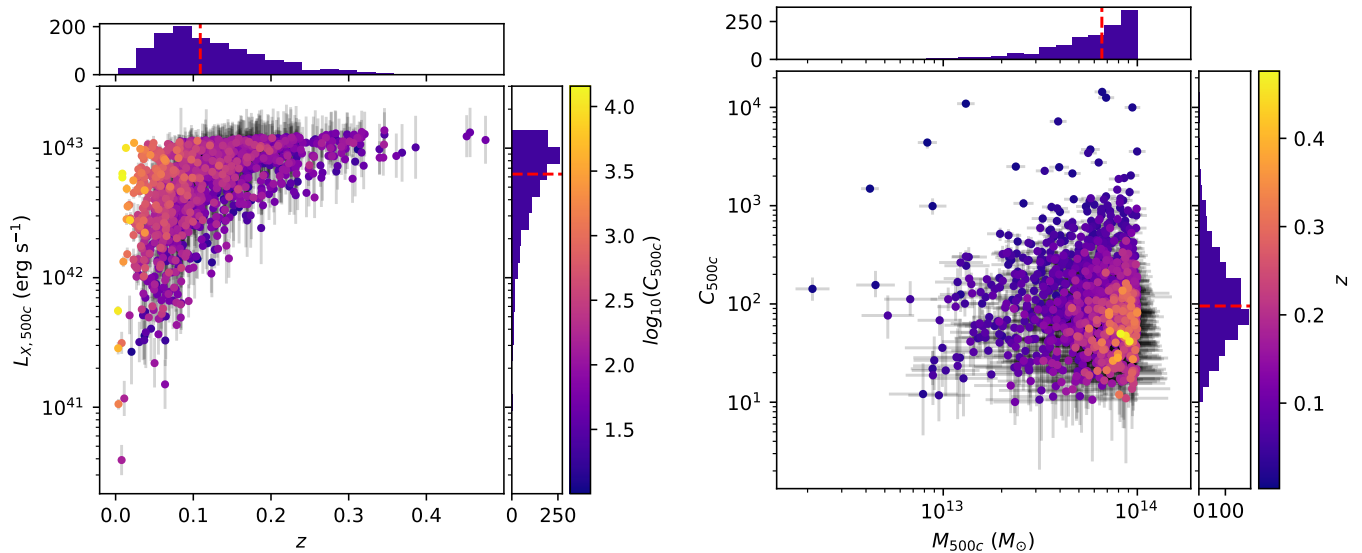


Fig. 5: *Left*: The soft-band (0.5–2 keV) X-ray luminosity ($L_{X,500c}$) and redshift (z) distributions of the galaxy group sample used in this work consist of 1178 objects. Luminosity of the groups cover a range of $3.9 \times 10^{40} - 1.4 \times 10^{43}$ ergs s^{-1} and the redshift span of the sample is 0.003 – 0.48. *Right*: Count (C_{500c}) and mass (M_{500c}) distributions of the 1178 galaxy group used in this work. Measured counts of galaxy groups range between 10 – 14380 and their masses span a range of $2.1 \times 10^{12} - 10^{14} M_{\odot}$. Median values of the $L_{X,500c}$, z , C_{500c} and M_{500c} observables are 6.3×10^{42} ergs s^{-1} , 0.11, 95, $6.5 \times 10^{13} M_{\odot}$ respectively.

The selection effects and the mass function need to be accounted for to obtain unbiased estimations of the physical properties of an underlying population from intrinsically scattered scaling relations. For this purpose, we built a Bayesian framework that simultaneously estimates the L_X and T , M_{500c} observables from the observed count-rate profiles, $\hat{C}_R(r)$ (see Sect. 3.2 for the details of the count-rate profile measurement procedure). The formulation of the Bayesian estimation framework is as follows. To simultaneously estimate L_X , T and M_{500c} observables, the joint probability density function, $P(L_X, T, M_{500c}|D, \theta_{\text{all}})$, given the data, D , and a set of model parameters, θ_{all} is needed to be computed. This can be expanded as:

$$P(L_X, T, M_{500c}|D, \theta_{\text{all}}) \equiv P(L_X, T, M_{500c}|\hat{C}_{R,500c}, I, z, \mathcal{H}, \theta_{\text{LT}}, \theta_{\text{LM}}) \quad (3)$$

where the count-rate within r_{500c} ($\hat{C}_{R,500c}$), detection information of the galaxy group (I), redshift (z), and sky position (\mathcal{H}), represent the data (D); and the scaling relations parameters (θ_{LT} and θ_{LM}) represent the model parameters (θ_{all}). We note that by definition, the $\hat{C}_{R,500c}$ term has an intrinsic dependence on M_{500c} such that $\hat{C}_{R,500c}$ is different for every M_{500c} in the $L_X - T - M_{500c}$ parameter space. Taking this into account, our framework allows all the information of the measured count-rate profiles to be included in our analysis rather than count-rate measurements within fixed radii.

Using the Bayes rule, Eq. 3 can be rewritten as

$$P(L_X, T, M_{500c}|\hat{C}_{R,500c}, I, z, \mathcal{H}, \theta_{\text{LT}}, \theta_{\text{LM}}) = \frac{P(L_X, T, M_{500c}, \hat{C}_{R,500c}, I|z, \mathcal{H}, \theta_{\text{LT}}, \theta_{\text{LM}})}{\int \int \int P(L_X, T, M_{500c}, \hat{C}_{R,500c}, I|z, \mathcal{H}, \theta_{\text{LT}}, \theta_{\text{LM}}) dL_X dT dM_{500c}} \quad (4)$$

Furthermore, one can expand the common term in the numerator and the denominator as

$$P(L_X, T, M_{500c}, \hat{C}_{R,500c}, I|z, \mathcal{H}, \theta_{\text{LT}}, \theta_{\text{LM}}) \approx P(\hat{C}_{R,500c}|L_X, T, M_{500c}, z) P(I|L_X, z, \mathcal{H}) \times P(L_X, T|M_{500c}, z, \theta_{\text{LT}}, \theta_{\text{LM}}) P(M_{500c}|z) \quad (5)$$

where the first term, $P(\hat{C}_{R,500c}|L_X, T, M_{500c}, z)$, stands for the measurement uncertainty of the count-rate. The conditional probability distribution for this term is obtained by first calculating the true count rate ($C_{R,500c}$) for every point in the $L_X - T$ parameter space by assuming the source emitting an unabsorbed APEC (Smith et al. 2001) spectrum in Xspec (Arnaud 1996) at a redshift z with an abundance of $0.3Z_{\odot}$, a temperature of T and a luminosity of L_X . Then the true count-rates ($C_{R,500c}$) are compared with the observed count-rates calculated ($\hat{C}_{R,500c}$) at every r_{500c} value in the mass parameter space (M_{500c}) and the value of the conditional probability is obtained. The $P(I|L_X, z, \mathcal{H})$ term in Eq. 5 is the selection function term that is a function of soft-band X-ray luminosity, redshift, and sky position where the sky position includes the local background surface brightness, exposure, and the neutral hydrogen column density information.

The selection function is obtained by simulating the eROSITA X-ray All-Sky observations using the baryon painting method (Comparat et al. 2019, 2020) and applying the same routines of the eSASS source detection pipeline to construct one-to-one correspondence of the catalogs and selection (Seppi et al. 2022; Clerc et al. submitted). The $P(M_{500c}|z)$ term is the mass function term for which the analytical formulation of Tinker et al. (2008) is used in this work. Lastly, the $P(L_X, T|M_{500c}, z, \theta_{\text{LT}}, \theta_{\text{LM}})$ term is the intrinsically scattered scaling relation term that gives the L_X and T distributions at a given mass and redshift.

Ideally, one would use a jointly fit, intrinsically scattered $L_X - T - M_{500c}$ scaling relation for the $P(L_X, T|M_{500c}, z, \theta_{\text{LT}}, \theta_{\text{LM}})$, however, there is no such relation in the literature yet that is calibrated by taking into account the selection effects and covers a

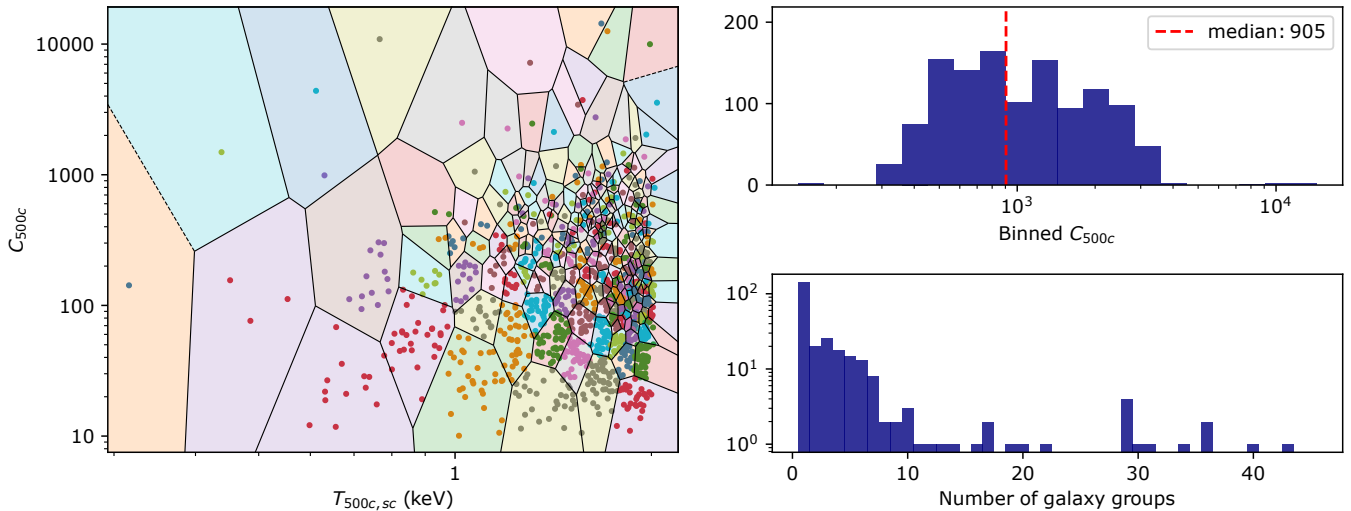


Fig. 6: *Left*: The Voronoi binning scheme used for grouping the sample obtained from the distribution of count (within r_{500c}) measurements (C_{500c}) and scaling relation based temperature estimates ($T_{500c,sc}$). *Top right*: The histogram of total counts in 271 Voronoi bins with a median of 905 counts. *Bottom right*: The histogram of galaxy groups in Voronoi bins.

similar mass range with eROSITA. For this reason, we expand this term as

$$P(L_X, T | M_{500c}, z, \theta_{LT}, \theta_{LM}) \approx P(T | L_X, z, \theta_{LT}) P(L_X | M_{500c}, z, \theta_{LM}) \quad (6)$$

and use the Bahar et al. (2022) $L_X - T$ and Chiu et al. (2022) $L_X - M_{500c}$ relations that are calibrated for eROSITA by taking into account the selection effects. The $P(T | L_X, z, \theta_{LT})$ term is obtained from $P(L_X | T, z, \theta_{LT})$ using Bayes theorem

$$P(T | L_X, z, \theta_{LT}) = \frac{P(L_X | T, z, \theta_{LT}) P(T | z)}{\int P(L_X | T, z, \theta_{LT}) P(T | z) dL_X} \quad (7)$$

where self-consistently, the same temperature function is used for the $P(T | z)$ term as in see Eq. 6 in Bahar et al. (2022).

As a final step, we substitute the terms in Eq. 5 to Eq. 4 and calculate the joint probability density function, $P(L_X, T, M_{500c} | \hat{C}_{R,500c}, l, z, \mathcal{H}, \theta_{LT}, \theta_{LM})$, for each galaxy group. Subsequently, we marginalize over the nuisance parameters and obtain L_X , T , and M_{500c} estimates given the data and the scaling relations parameters⁷. We provide the distributions of mass, temperature, soft-band (0.5 – 2 keV) X-ray luminosity estimates obtained through this Bayesian framework along with the distributions of redshift and count (0.3 – 1.8 keV) of the final galaxy group sample in Figs. 1, 5 and 6.

The estimated M_{500c} are then converted to r_{500c} and r_{2500c} by assuming an average dark matter concentration of $c_{500c} = r_{500c}/r_{s,NFW} = 4.2$ ⁸ and scaling the r_{500c} estimates accordingly (S09). These characteristic radii are employed to determine the

⁷ For example, the marginal probability distribution of temperature is calculated as $P(T | \dots) = \iint P(L_X, T, M_{500c} | \dots) dL_X dM_{500c}$ and the temperature corresponding to the 50th percentile of the marginal probability distribution is used as the point estimate.

⁸ $r_{s,NFW}$ is the characteristic radius of the Navarro–Frenk–White (NFW) profile and a concentration (c_{500c}) of 4.2 corresponds to a r_{2500c}/r_{500c} ratio of 0.465.

spectral extraction region ($r < r_{500c}$) and serve as characteristic radii ($0.15r_{500c}$, r_{2500c} , r_{500c}) for the entropy measurements.

3.4. Grouping and the Spectral Analysis

Measuring temperature through X-ray spectroscopy requires considerably more photons than measuring surface brightness properties with imaging analysis. Given the shallow nature of the eROSITA All-Sky Survey, the photon counts of most of the galaxy groups in our sample are insufficient for temperature measurements, even though the flux or luminosity of these objects can be reliably measured from X-ray images. For instance, more than half of the groups in the sample, shown on the right panel of Fig. 5, have less than 100 counts within the 0.3–1.8 keV band that is not sufficient for measuring their temperature reliably.

The two canonical ways to overcome the problem of insufficient photon counts for spectral analysis are co-fitting or stacking. A plethora of examples of both techniques exist in the literature. For example, McDonald et al. (2014) co-fit radially extracted spectra of 80 South Pole Telescope (SPT) selected massive clusters, while Bulbul et al. (2014) and Zhang et al. (in prep.) stacked megaseconds of XMM-Newton and eROSITA spectra respectively to achieve a high signal-to-noise level and reveal faint spectral features. In this work, we employ the co-fitting technique to maintain the spectral information of individual groups that would be averaged out when stacked. This method is the most suitable for the primary goal of this work. Compared to stacking, this approach is computationally expensive; however, with the recently developed high-performance Central Processing Units (CPUs) and the improvements in parallel computing, we are able to employ the co-fitting technique in this work.

We group the sample such that the IGrM temperatures of the galaxy groups are similar in each bin. Moreover, we require the statistical constraining power (photon counts) of the groups in the same bin to be similar to each other to avoid the source with the highest count biasing the measurements. In other words,

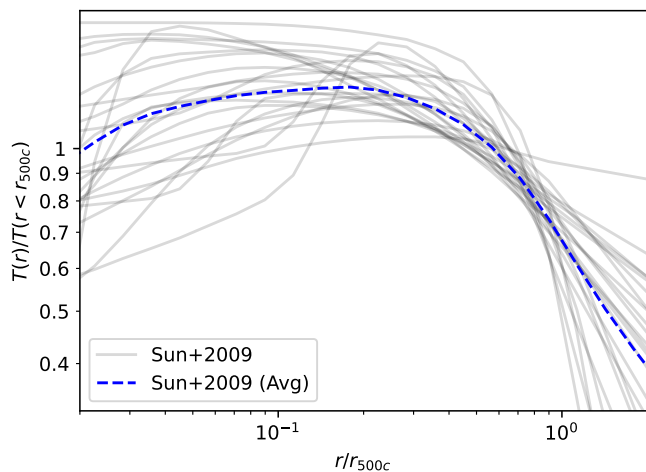


Fig. 7: Normalized temperature profiles, $T(r)/T(r < r_{500c})$, of 23 groups (gray) presented in S09 and their average (blue). The blue dashed line provides an average conversion ratio between the temperature profile, $T(r)$, and the characteristic temperature measurements, $T(r < r_{500c})$.

we aim to minimize the temperature and photon count variation ($\Delta T_{500c} \sim std(T_{500c})$ ⁹ and $\Delta C_{500c} \sim std(C_{500c})$) in each bin while trying to achieve a sufficient signal-to-noise ratio. To achieve this, we group the sample using the Voronoi binning technique (Cappellari & Copin 2003). To apply the tessellation technique, we pixelate our temperature proxy $T_{500c,sc}$ (surface brightness inferred temperature estimate; see Sect. 3.3 for the details) and count measurements C_{500c} such that each pixel occupied by only one galaxy group. The axes are then re-scaled, and the resulting image is given to the *Vorbin* package, the Python implementation of the Voronoi binning technique. The free parameters, namely, the axes scaling factors and the target SNR, are fine-tuned until the temperature variation (ΔT_{500c}) and the photon count variation (ΔC_{500c}) in the Voronoi bins are sufficiently small. The final binning scheme, shown in Fig. 6, is achieved using an SNR target, $S/N = 22.36$ (equivalent to 500 counts). We further present the distributions of the total counts and the number of galaxy groups in the Voronoi bins in Fig. 6. Using this binning scheme, we obtained 271 bins with a median count of 905, sufficient for obtaining reliable spectroscopic temperature measurements at $T < 2$ keV for each bin. We note that the binning scheme can be slightly different if a different target SNR or axis scaling factors are chosen; however, the impact of the chosen binning scheme is negligible on the final results as long as the resulting ΔT_{500c} and ΔC_{500c} are similar.

After the grouping, the source and local background spectra of the galaxy groups in our sample are extracted using the eSASS task, *srctool*. The source spectra are extracted from the circular regions centered around the galaxy group and have a radius of r_{500c} (see Sect. 3.3 for the details of the M_{500c}/r_{500c} estimation procedure). Similarly, the local background spectra are extracted from annuli that are centered around the galaxy group and have a radial range of $4r_{500c} < r < 6r_{500c}$. The best-fit count-rate profiles are used to determine the masking radius of the bright point sources and nearby extended objects co-fitted during the imaging analysis. The remaining point sources and nearby extended

⁹ The notation $std(X)$ represents standard deviation of X .

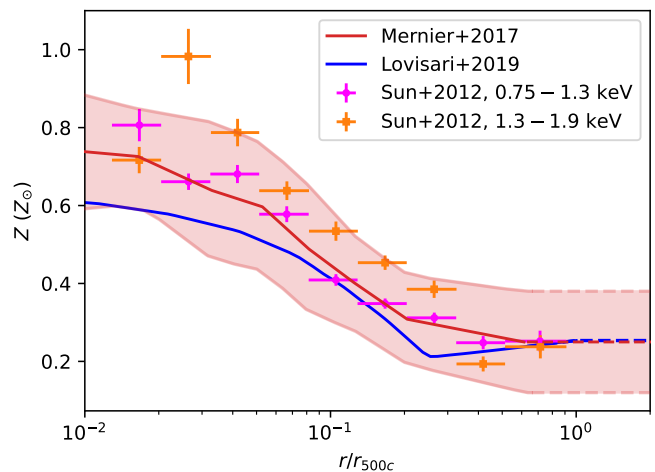


Fig. 8: Average metallicity profiles of galaxy groups reported by Mernier et al. (2017), Lovisari et al. (2015) and the stacked metallicity profiles of Sun (2012) for galaxy groups in two temperature bins ($T = 0.75 - 1.3$ keV and $0.75 - 1.3$ keV).

sources within the extraction region are masked as described in Sect. 3.2.

We extract ancillary response files (ARFs) and redistribution matrix files (RMFs) using the *srctool* task for the background and the source region in different settings to be assigned to various components of the source and background models. The ARF assigned to the source component is extracted with the *exttype=BETA* and *psftype=2D_PSF* settings to consider the energy-dependent PSF and vignetting corrections. Over the extraction regions, the flux distribution of the vignettted X-ray background is assumed to be flat, and the *exttype=TOPHAT* and *psftype=NONE* settings are used for extracting the ARFs assigned to the vignettted X-ray background components of the source and background regions.

Similar to our eFEDS analysis (Ghirardini et al. 2021; Liu et al. 2022; Bahar et al. 2022; Bulbul et al. 2022), the local background model consists of two major components: particle-induced instrumental background (see Bulbul et al. 2020; Freyberg et al. 2020, for further details) and X-ray background including the Galactic foreground, and unresolved point sources in the sky. The total model includes a spectral model component with an absorbed thermal component. The spectral analysis is performed using PyXspec, the Python interface of the standard X-ray spectral analysis package Xspec (version 12.12.1, Arnaud 1996). The Xspec model of the X-ray foreground consists of an unabsorbed APEC (Smith et al. 2001) for the local hot bubble (Yeung et al. 2023, $T \sim 0.084$ keV), two absorbed APECs for the hot and cold components of the galactic halo (Ponti et al. 2023; Bulbul et al. 2012, $T \sim 0.49$ and 0.157 keV respectively). To model the cosmic X-ray background, we use an absorbed power-law for the unresolved AGN (Cappelluti et al. 2017, $\Gamma = 1.45$). For the shape of the instrumental background, we use the best-fitting model of Yeung et al. (2023) obtained by calibrating the filter wheel closed (FWC) data (see Appendix A.1. and A.2. of Yeung et al. 2023, for the details of the modeling of FWC data). This instrumental background component is folded with unvignettted ARF (Freyberg et al. 2020), while the cosmic X-ray background and Galactic foreground are folded with the respective vignettted ARF in the fits.

To account for the X-ray absorption, we use the TBABS (Wilms et al. 2000) interstellar medium (ISM) absorption model in Xspec (Arnaud 1996). We use the HI4PI survey (HI4PI Collaboration et al. 2016) for calculations of the hydrogen column density (n_{H}). The n_{H} values at the positions of eRASS1 galaxy groups are relatively low because of their locations at higher Galactic latitudes; therefore, using the total hydrogen column density ($n_{\text{H,tot}}$) rather than the neutral hydrogen column density ($n_{\text{H,I}}$) does not have a significant impact on our results as noted in Bulbul et al. (submitted). We use the solar abundances of Asplund et al. (2009) when measuring the metallicity of the groups. We use C-statistic (Cash 1979) for the statistical interpretation of our spectra that provides unbiased estimates of the model parameters at the low and high count regimes (Kaastra 2017). We employ the co-fitting technique for the spectral analysis. This requires us to explore likelihoods with relatively high dimensional parameter space. For this purpose, we have chosen to employ the MCMC fitting technique. Xspec has a built-in MCMC sampler; however, the control it allows the user over the priors is limited. For this reason, we employ the widely used MCMC sampler emcee (Foreman-Mackey et al. 2013) rather than the built-in Xspec sampler to explore high dimensional likelihoods. We achieved this by developing an interface that allows the cross-talk between PyXspec and emcee and updates the model parameters at every MCMC step accordingly.

Galaxy groups are low-mass objects with relatively low plasma temperatures ($T < 2$ keV) due to their shallower potential wells. They share this low-temperature parameter space with other background/foreground components, such as the cold ($T \sim 0.157$ keV) and hot ($T \sim 0.49$ keV) components of the galactic halo (Ponti et al. 2023). This results in degeneracies between the source and background/foreground components at the low count regime. At a given energy band, it is relatively easy to separate the source and background components using the 2D distribution of photons through imaging analysis since we expect the local background rate to be relatively flat, whereas the source emission roughly follows a projected Vikhlinin profile (Vikhlinin et al. 2006). In this work, we make use of this fact and combine the spatial and spectral information of photons following a novel approach with the aim of lifting the aforementioned degeneracies the best we can. We achieve this by using the observed count-rates (0.3–1.8 keV) measured through imaging analysis as priors in the spectral analysis in our pipeline that combines PyXspec and emcee.

To obtain the average temperatures of the binned galaxy groups (see the first paragraph of this section for the details of the grouping), we only link the temperature parameter of the (APEC) model and co-fit all the source and background spectra of the galaxy groups in each Voronoi bin. In total, $2 \times N_{i,\text{gr}}$ spectra are co-fit (one spectrum for the source region and one for the background region) where $N_{i,\text{gr}}$ is the number of galaxy groups in the i 'th Voronoi bin. During the fitting, the temperatures, the normalizations of the X-ray background components, and the normalizations of the unvignetted particle background components are allowed to be free with flat priors in the logarithmic parameter space.

Many studies in the literature show strong degeneracy between the temperature and metallicity measurements for galaxy clusters and groups hosting multi-phase gas. This manifests as the so-called 'Fe bias' (Buote & Fabian 1998; Buote 2000; Gastaldello et al. 2021; Mernier et al. 2022) where temperature and abundance measurements change depending on the number of gas components fitted. In our work, we take this effect into account by allowing the metallicities of each galaxy group to

be free with a Gaussian prior centered around $0.3 Z_{\odot}$ with a standard deviation of 0.025 while measuring average temperatures. The normalization of the source emission of each galaxy group and the co-fit temperature are left free with log-uniform priors. Consequently, following the spectral co-fitting analysis procedure described above, we obtained 271 average temperature measurements within r_{500c} for each Voronoi bin shown in Fig. 6.

3.5. Electron Density, Temperature, and Entropy Profiles

From the imaging analysis described in Sec.3.2, we obtain deprojected emissivity profiles of all the 1178 galaxy groups. The spectral analysis, described in Sec.3.4, yields average temperature measurements of the 271 galaxy group bin within r_{500c} . The electron number density profile measurements of the IGrM have a non-negligible dependence on the assumptions on the temperature and metallicity profiles. Furthermore, temperature profiles of the galaxy groups are needed for obtaining entropy profiles. For most binned groups, only a single average temperature and metallicity measurement can be achieved within r_{500c} due to low SNR eROSITA data. We overcome this limitation and incorporate the impact of temperature variation on the thermodynamic properties as a function of radius, as described below.

To account for the radial temperature variation, we first determine the average shape of the 3D temperature profile of groups ($T(r)/T(r < r_{500c})$) using the temperature profile measurements of the tier 1 and 2 groups presented in S09 (see Sect. 4.1 for the details). The average and individual shapes of the $T(r)/T(r < r_{500c})$ profiles are shown in Fig. 7. We then rescale the average shape with the integrated temperature measurements and obtain the average temperature profiles for each binned group. The temperature profile measurements presented in S09 for a sample of 43 groups are obtained by analyzing deep *Chandra* observations; therefore, the overall shape of the profiles is relatively well-constrained. Following this procedure, we obtain the average temperature profiles of the 271 galaxy group bins. We note that our approach of obtaining temperature profiles of groups is equivalent to fixing the shape of an assumed temperature profile and fitting spectra by allowing the normalization of the profile to be free. We further note that the observed temperature measurement discrepancy between telescopes does not affect our work given that the temperature measurements of eROSITA for galaxy groups agree very well with the *Chandra* and XMM-Newton temperatures (Migkas et al. submitted).

For the metallicity profile, we consider the following studies in the literature that have reasonably large galaxy group samples: Sun (2012), Mernier et al. (2017), and Lovisari & Reiprich (2019). We find that their measurements agree relatively well within the scatter of the metallicity profile reported in Mernier et al. (2017) (see Fig. 8). For this reason, we adopt the median Mernier et al. (2017) metallicity profile (Z_{M17}) for our measurements and consider the scatter of their profile as our systematic uncertainty. We quantify the impact of this uncertainty on the thermodynamic profile measurements ($n_e(r)$ and $S(r)$) and consider the resulting difference as part of the overall error budget (see Sect. 4.1 for the details of the assumed metallicity profile and quantification of the impact of this choice).

We then calculate the electron density profiles from our deprojected emissivity measurements by constructing APEC models in Xspec (similarly done in Liu et al. 2022) having the temperatures equal to the temperature profiles of the binned groups and the metallicities equal to the assumed metallicity profile at all radii out to $2r_{500c}$. During the n_e profile calculation, in addition

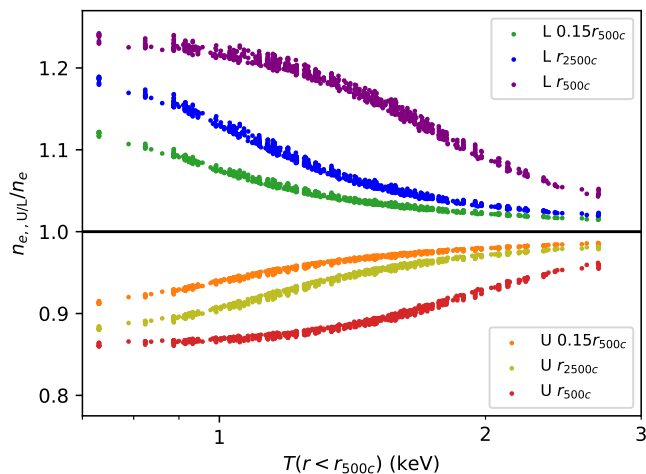


Fig. 9: Ratio of the electron densities obtained by assuming low/up-scattered Mernier et al. (2017) metallicity profiles to the electron densities obtained by the median Mernier et al. (2017) metallicity profile at three radii, $0.15r_{500c}$, r_{2500c} and r_{500c} as a function of characteristic temperature, $T(r < r_{500c})$. Green, blue, and purple data points represent the ratio between the electron densities obtained by assuming the lower envelope ($n_{e,L}$) of the red shared area and the dark red median line (n_e) in Fig. 8. Orange, yellow, and red data points represent the ratio between the electron densities obtained by assuming the upper envelope of the red shared area ($n_{e,U}$) and the dark red median line (n_e) in Fig. 8.

to the errors of the imaging analysis, the uncertainties of the average metallicity and temperature measurements are propagated as well using the MCMC chains of the spectral analysis, taking into account the covariances. Then, the electron density profiles of the objects within each Voronoi bin are averaged to get the average electron density profiles of the binned groups.

Lastly, the entropy profiles of the binned groups are obtained by combining the average electron density and the temperature profiles using the equation below.

$$S(r) = T(r)/n_e(r)^{2/3}. \quad (8)$$

The entropy profiles are then sampled at three characteristic radii, and the final entropy measurements of 271 galaxy group bins are obtained. The full shape of the entropy profiles of binned groups, along with the other thermodynamic profiles such as electron density and pressure ($P = n_e T$), will be presented in Bahar et al. (in preparation).

Besides the systematics resulting from the metallicity profile, we also consider other major systematics that have a non-negligible impact on the thermodynamic properties measured in this work. We discuss and quantify the impact of these systematics on our measurements in Sect. 4 and take them into account as part of the total error budget when we draw conclusions in the next section.

4. Assumptions, Corrections, and Systematics

Having fair comparisons between the thermodynamic properties of groups observed with different X-ray observatories and simulations is a challenging task as various systematics should be

taken into account in the measurements, such as the systematic uncertainties on the metallicity and temperature profiles, systematic uncertainties on the group masses and the flux calibration between instruments.

4.1. Assumptions on Temperature and Metallicity Profiles

Accounting for the temperature and metallicity radial variation is key to having reliable thermodynamic profiles. Shallow survey observations and low signal-to-noise data of most groups in our sample are insufficient to measure temperature profiles reliably. There are various studies in the literature on the average temperature profile of the hot gas in clusters (e.g., McDonald et al. 2014; Ghirardini et al. 2019), while the studies focusing on the shape of the average temperature profile of groups with a large enough sample are limited. An in-depth study of 43 nearby galaxy groups with deep *Chandra* observations by S09 (among which 23 of them have good temperature constraints out to r_{500c}) is one of the few studies we compare within this work. In this work, we use the temperature profile measurements of these 23 groups to get the average shape of the temperature profile of groups. To get the average shape, we first calculate the characteristic temperatures of the groups, $T(r < r_{500c})$, by projecting and integrating all the temperature profiles within a cylindrical volume of radius r_{500c} . We achieve this following the Mazzotta et al. (2004) weighting and projection formulas

$$w = n_e n_p T^\alpha \quad (9)$$

and

$$T_{sl} = \frac{\int w T dV}{\int w dV} \quad (10)$$

where for α we use 0.76 that is calibrated for eROSITA (ZuHone et al. 2023). Furthermore, we use our average group electron density profile for n_e (Bahar et al. in preparation). We then divide the temperature profiles with the characteristic temperatures and obtain the normalized temperature profiles, $T(r)/T(r < r_{500c})$. Lastly, we take the average of these profiles and renormalize them to get the average shape of the temperature profiles of groups. The average and individual normalized profiles of 23 groups are shown in Fig. 7.

Unlike clusters, the band-averaged cooling function of groups has a strong metallicity dependence because of the significant contribution from the line emission at temperatures, $T < 2$ keV. Therefore, the radial change in metallicity from the center to the outskirts should be accounted for to calculate electron density profiles accurately.

During the last decade, the shape and the strength of emission lines have significantly changed in most commonly used plasma emission codes (see Fig. 1 in Gastaldello et al. 2021) that had a strong influence on the metallicity measurements of groups (e.g., Mernier et al. 2018). For this reason, it is important to use the most recent publications and account for uncertainties in metallicity profiles in the systematics error budget. Among the metallicity profile measurements in the literature, the results presented in Sun (2012), Mernier et al. (2017) and Lovisari & Reiprich (2019) stand out as the most recent studies with moderately large galaxy group samples with sufficiently deep observations. Fig. 8 presents the stacked metallicity profiles of Sun (2012) and the average metallicity profiles of Mernier et al. (2017) and Lovisari & Reiprich (2019) that are renormalized based on the iron abundance ratio of Asplund et al. (2009). In Sun (2012), the author reports stacked abundance profiles of

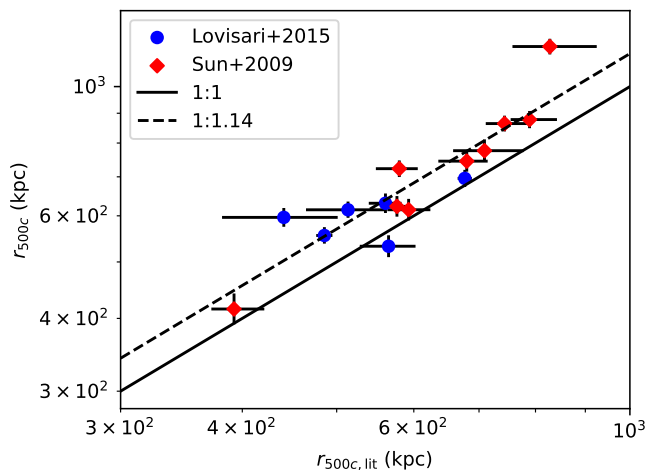


Fig. 10: Comparison between the scaling relation based r_{500c} estimates of the cross-matched galaxy groups obtained in this work (y-axis: r_{500c}) with the literature estimates (x-axis: $r_{500c,lit}$) obtained by assuming hydrostatic equilibrium (Sun et al. 2009; Lovisari et al. 2015).

39 galaxy groups in three temperature bins (0.75 – 1.3, 1.3 – 1.9 and 1.9 – 2.7 keV). In this work, we consider only the results of the first two temperature bins (0.75 – 1.3 keV and 1.3 – 1.9 keV), which are relevant to our sample that has a median temperature of $T(r < r_{500c}) = 1.45$ keV.

Overall, the average metallicity profile reported in Mernier et al. (2017) lies between the Sun (2012) and Lovisari & Reiprich (2019) measurements and the Sun (2012) measurements in the 1.3 – 1.9 keV temperature bin lies above the Mernier et al. (2017) profile and the average measurements of Lovisari & Reiprich (2019) lie below the Mernier et al. (2017) profile. When calculating the thermodynamic properties, the differences in metallicity measurements must be accounted for as systematics because of the strong dependence of emissivity on metallicity at group scales. Given the large spread of metallicity measurements, we take the average profile of Mernier et al. (2017) as our default profile and conservatively consider the shaded area as the systematics of the average profile measurements. To account for the impact of the choice of average metallicity profile, we construct APEC spectra in Xspec and obtain deprojected electron density profiles of the 1178 galaxy groups in our sample (similarly done in Liu et al. 2022) using the scaled temperature profiles and three metallicity profiles (low-scattered, median, and up-scattered Z_{M17} profiles) shown with red in Fig. 8. We present the ratios of the electron densities in Fig. 9 that are obtained by using the aforementioned three metallicity profiles (low-scattered Z_{M17} : $n_{e,L}$, median Z_{M17} : n_e , and up-scattered Z_{M17} : $n_{e,U}$) for 1178 groups at the three characteristic radii ($0.15r_{500c}$, r_{2500c} and r_{500c}). The ratios ($n_{e,U}/n_e$ and $n_{e,L}/n_e$) ranging between 0.84 – 1.24 in Fig. 9 indicating a non-negligible difference between the electron density measurements. The ratios deviate more from unity as the characteristic temperature decreases, and the measurement radius increases. This is due to line emission, coupled with metallicity, which plays a more important role as the temperature decreases. The procedure described above is followed for the final results, and the radius/temperature dependent systematics due to the choice of metallicity profile are quantified and propagated to our final entropy measurements presented in Sect. 5.

4.2. Correction for the Flux Discrepancy

A discrepancy of 15% is reported in the luminosity measurements in the soft-band (0.5 – 2 keV) of a subsample of massive galaxy clusters observed with both eROSITA and *Chandra* (Bulbul et al. submitted). The observed flux difference is constant with no flux or luminosity dependence. Some of this difference can be explained by the photon loss in the latest processing due to the higher CCD thresholds (Merloni et al. 2024); however, further investigation is required to understand the observed flux discrepancy, which could be due to various calibration effects. We account for the flux discrepancy while comparing our entropy measurements with those reported in the literature. Among our two main X-ray observables n_e and T , only electron density is impacted by the flux discrepancy since the spectroscopic T measurements are not sensitive to the overall flux normalization. To roughly estimate the impact, we assumed the shape of the measured electron density profile to be the same for different instruments, used the fact that $L \propto n_e^2$, and obtained a ratio of $n_{e,eRO}/n_{e,Cha} = 0.85^{0.5} \sim 0.92$ between the electron density measurements of *Chandra* and eROSITA. The 8% underestimation of n_e corresponds to a 5% overestimation of entropy. This fraction is factored in the *Chandra* measurements in S09 when comparing with the eROSITA results in Fig. 14.

4.3. Systematics Related to Mass Measurements

We note that entropy measurements at overdensity radii, $0.15r_{500c}$, r_{2500c} , and r_{500c} are sensitive to the assumed masses of the galaxy groups. This dependence is due to the entropy profile of galaxy groups being a strong function of the radial distance and the overdensity radius, which is a mass-dependent quantity (e.g. Bulbul et al. 2010; Ghirardini et al. 2019). Therefore, any disagreement in radius and mass may lead to a bias in the measured thermodynamic profiles and their comparisons between different methods. Masses of galaxy groups can be estimated in different ways, such as by assuming hydrostatic equilibrium, using the shear information of the lensed galaxies, or using scaling relations; however, these methods have advantages and disadvantages along with introduced biases. Comparison of the mass estimation techniques for galaxy groups is beyond the scope of this paper; therefore, in this paper, we account for the bias introduced while comparing our results with the literature. We find that our scaling relations based r_{500c} estimates are $\sim 14\%$ higher than the hydrostatic equilibrium based r_{500c} estimates in S09 for 9 cross-matched groups. Furthermore, we cross-match and compare our group catalog with the galaxy group sample used in Lovisari et al. (2015) and found a similar difference between our r_{500c} estimates with their hydrostatic equilibrium-based r_{500c} measurements for 6 groups. Comparison between our characteristic radii estimates (r_{500c}) and those in the literature ($r_{500c,lit}$) is provided in Fig. 10. An discrepancy of $\sim 14\%$ approximately corresponds to a bias of $\sim 48\%$ ($1.14^3 = 1.48$) on M_{500c} . This result agrees with the 45% hydrostatic mass bias observed in galaxy groups (Nagai et al. 2007), see also Sect. 6.2 of S09. We note that constraining hydrostatic mass bias, especially in galaxy groups, is challenging due to our limited knowledge of the magnitude of non-thermal pressure support, magnified in galaxy groups due to powerful AGN feedback compared to galaxy clusters. Moreover, the fraction of discrepancy may be due to other systematics in the measurements, such as the representation of the $L_X - M$ relation with a single power-law spanning a large mass range. We provide the r_{500c} estimates of the 15 cross-matched groups with S09 and Lovisari et al. (2015) in

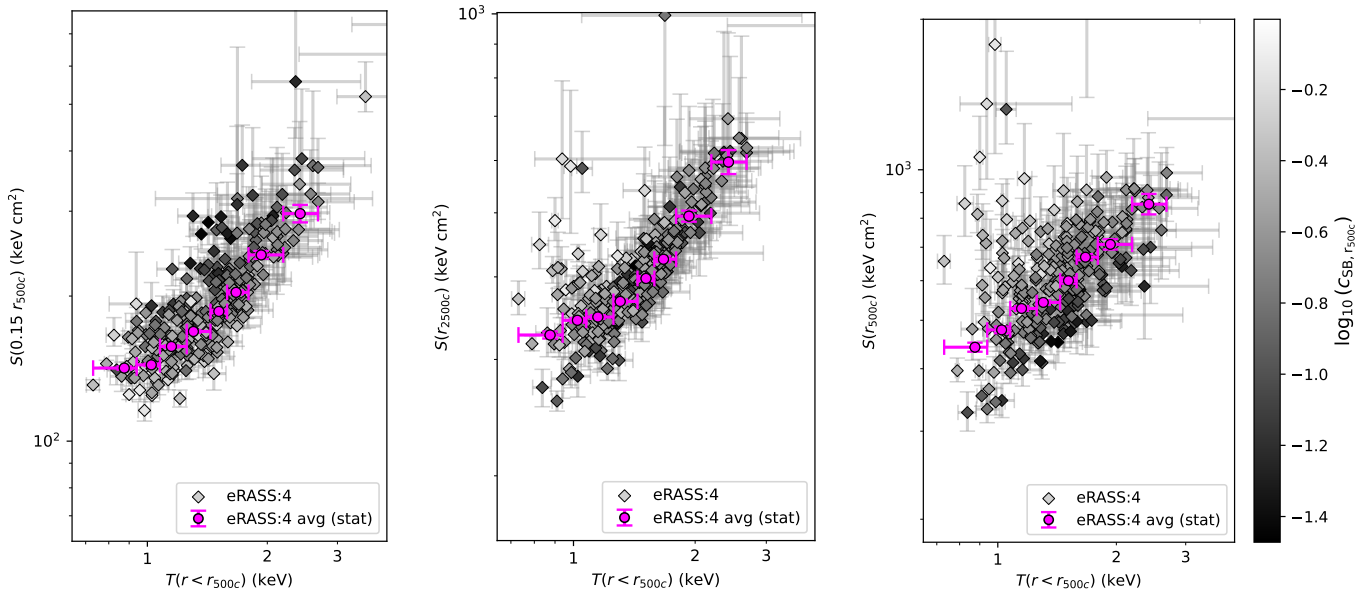


Fig. 11: Average entropy measurements of binned groups (diamonds) at three radii ($0.15r_{500c}$, r_{2500c} , r_{500c}) as a function of characteristic temperature, $T(r < r_{500c})$. The colors of the diamond data points represent the average concentration ($c_{\text{SB}, r_{500c}} = SB(r < 0.1r_{500c})/SB(r < r_{500c})$) of the groups within the corresponding Voronoi bin. Error-weighted averages of the diamond data points are shown in magenta.

Table 1: Positions, redshifts and r_{500c} estimates of the crossmatched groups.

eROSITA ID (1eRASS)	Literature name	RA* (deg)	DEC* (deg)	z^*	r_{500c}^\dagger (kpc)
J120427.3+015346	MKW4	181.114	1.896	0.0203	723
J093325.7+340302	UGC 5088	143.357	34.051	0.0269	415
J120638.9+281024	NGC 4104	181.662	28.173	0.0283	623
J110943.5+214545	A1177	167.432	21.763	0.0322	615
J054006.9-405004	ESO 306-017	85.029	-40.835	0.0368	864
J000313.1-355607	A2717	0.805	-35.935	0.0500	878
J102212.8+383136	RXJ 1022+3830	155.553	38.527	0.0544	745
J231358.6-424338	AS1101	348.494	-42.727	0.0557	1172
J131214.0-005825	A1692	198.059	-0.974	0.0843	776
J140341.9-340022	S0753	210.925	-34.006	0.0132	532
J184717.9-631952	S0805	281.825	-63.331	0.0143	596
J105026.1-125037	NGC 3402	162.609	-12.844	0.0154	555
J024933.9-311126	S0301	42.392	-31.191	0.0228	614
J045452.7-180642	CID28	73.720	-18.112	0.0317	696
J062439.9-372011	A3390	96.166	-37.337	0.0334	631

Notes. The information presented in the first 9 rows is for the groups crossmatched with S09, and the information presented in the last 6 rows is for the groups crossmatched with [Lovisari et al. \(2015\)](#).

* RA, DEC, and z of the listed groups are taken from [Bulbul et al. \(submitted\)](#).

† Scaling relation based r_{500c} estimates used in this work are obtained by fully accounting for the selection and the mass functions.

Table 1 along with the slopes of the average entropy profiles of the binned groups at the three characteristic radii in Table 2.

The mass estimate dependence is also responsible for the observed scatter in the entropy of the sample. Fig. 11 shows a strong correlation between the scatter of the average entropy measurements at a given temperature and the average concen-

tration ($c_{\text{SB}, r_{500c}} = SB(r < 0.1r_{500c})/SB(r < r_{500c})$) of the sample (see [Sanders et al. in prep.](#), for the concentration measurements). This is expected since the M_{500c} (or r_{500c}) estimates used in this work are obtained using an $L_X - M$ scaling relation. At a given mass, the cool-core galaxy groups with higher luminosity would have higher entropy measurements while the

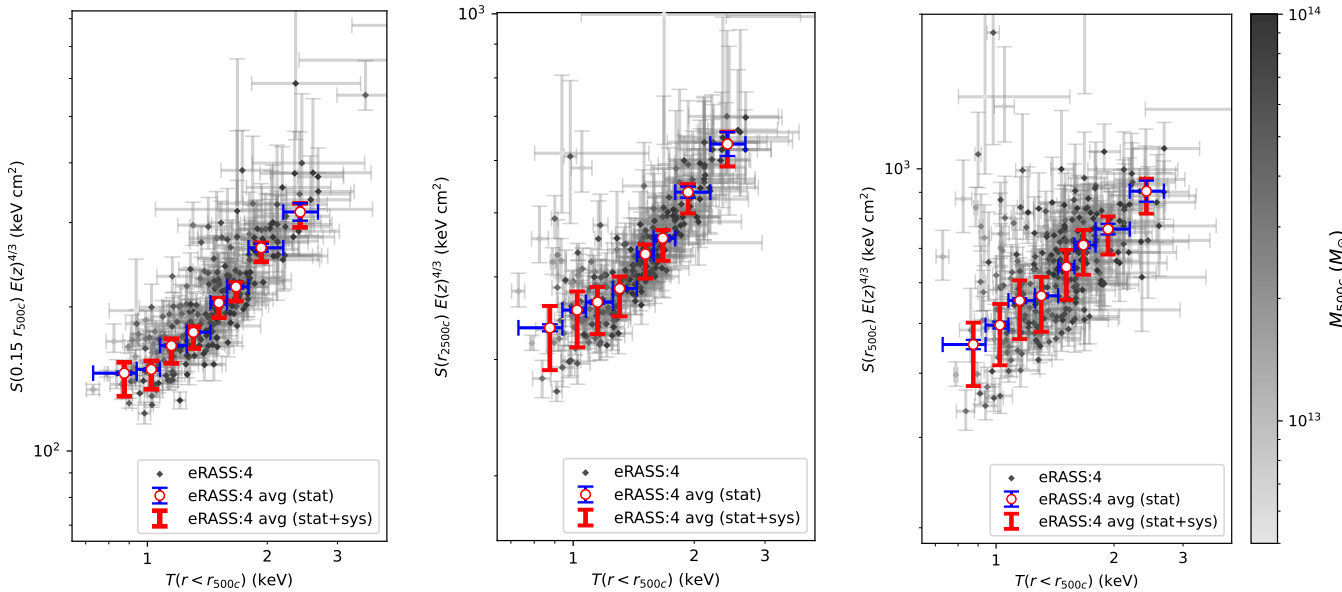


Fig. 12: Redshift evolution scaled average entropy measurements of binned groups (grey diamonds) at three radii ($0.15r_{500c}$, r_{2500c} , r_{500c}) as a function of characteristic temperature, $T(r < r_{500c})$. The colors of the grey data points represent the average masses (M_{500c}) of the groups within the corresponding Voronoi bin. Error-weighted averages of the data points are plotted as white circles, statistical uncertainties of the averages are shown with blue error bars, and the overall error budget of the average measurements resulting from the statistical and systematic uncertainties are shown with red error bars (see Sect. 4 for the details of the accounted systematics).

others scatter around the sample's median. The average entropy and temperature measurements of the sample are presented in Fig. 11, where the colors of the data points indicating average concentration obtained by averaging the measurements provided in Sanders et al. (in prep.). A few extreme cases with larger concentration, electron number density, and entropy are easily noticeable in Fig. 11. By construction, the r_{500c} (or M_{500c}) estimates are, on average, unbiased at the sample scale. Therefore, a small scatter does not significantly impact the conclusions in this work. On average, these effects cancel out such that at all three radii, the error-weighted average entropy plotted in magenta coincides with the intermediate concentration values $\log_{10}(c_{SB,r_{500c}}) \sim -0.7$.

5. Entropy and Characteristic Temperature Measurements

In this work, we constrain the entropy of the IGrM, utilizing the deep eRASS:4 observations of the galaxy groups detected in the eRASS1 survey. In this section, we present our measurements of the characteristic temperature, $T(r < r_{500c})$, and entropy at three overdensity radii, $0.15r_{500c}$, r_{2500c} , and r_{500c} , from the combined analysis of 1178 galaxy groups. We then compare our findings with the previously reported results in the literature.

Following the procedures described in Sects. 2 and 3, we obtain average entropy and temperature measurements of a sample of 1178 eROSITA selected galaxy groups in 271 bins. Our measurements for the average temperature and average entropy at three characteristic radii scaled by the self-similar redshift evolution ($E(z)^{4/3}$) can be seen in Fig. 12, where the error-weighted average entropy measurements are shown in white circles, the statistical uncertainties are shown with blue errorbars and the overall error budget resulting from the statistical and systematic (see Sect. 4) uncertainties are shown with red error bars. Error-

weighted average of the redshift evolution scaled entropy measurements, their statistical uncertainties, and the impact of systematics are also provided in Table 2 as a function of IGrM temperature. Besides the average entropy measurements, we provide slopes of the average entropy profiles in Table 2 at the three characteristic radii for future work to account for the mass measurement systematic while comparing with our results (see Sect. 4.3 for the details of accounting the systematics in mass measurements). We note that the few outlying entropy measurements in Fig. 12 are due to the extreme cool-core objects and have negligible impact on our error-weighted entropy measurements (see Sect. 4.3 for a more detailed discussion on the outliers and their impact on our final results).

We find that the characteristic temperature measurements of our binned group sample span a range of $\sim 0.73 - 2.68$ keV. Furthermore, we find that the characteristic temperature measurements of the binned groups correlate well with the entropy measurements at the three characteristic radii such that, an increase in the characteristic temperature from 0.73 keV to 2.68 keV corresponds to an increase from the redshift scaled entropy levels of 121, 271, 341 keV cm² to 404, 722, 1135 keV cm² respectively. This trend can also be clearly seen from the error-weighted average measurements (white circles) in Fig. 12 such that the error-weighted averages at these three radii increase from the levels of 145, 335, 455 keV cm² to 316, 635, 905 keV cm² respectively. It can further be noticed that as the characteristic temperature of the binned groups decreases, the statistical uncertainty of the error-weighted average profiles (blue error bars) decreases. Conversely, the decrease in the temperature corresponds to an increase in the overall error budget (red error bars). This is due to the fact that the line emission from the Fe-L complex at the low-temperature parameter space becomes significant, which provides an additional spectral feature for measuring the temperature and reduces the statistical uncertainty. Meanwhile, at the

Table 2: Average entropy, and entropy slope measurements of the grouped sample as a function of temperature at the three characteristic radii: $0.15r_{500c}$, r_{2500c} , and r_{500c} .

	$T(r < r_{500c})$ (keV)							
	0.73 – 0.94	0.94 – 1.08	1.08 – 1.26	1.26 – 1.44	1.44 – 1.59	1.59 – 1.79	1.79 – 2.19	2.19 – 2.68
$S(0.15r_{500c})E(z)^{4/3*}$	$145.4^{+1.1(+7.7)}_{-1.1(-15.3)}$	$148.09^{+0.90(+6.1)}_{-0.89(-13.5)}$	$166.04^{+0.87(+5.5)}_{-0.86(-13.6)}$	$177.0^{+1.2(+4.6)}_{-1.2(-13.2)}$	$203.9^{+1.6(+4.3)}_{-1.6(-14.0)}$	$220.2^{+2.1(+3.9)}_{-2.0(-14.4)}$	$265.8^{+5.0(+3.9)}_{-4.9(-16.5)}$	$316^{+13(+3.6)}_{-13(-18.6)}$
$S(r_{2500c})E(z)^{4/3*}$	$335.0^{+4.1(+26)}_{-4.1(-46)}$	$356.3^{+2.9(+24)}_{-2.9(-43)}$	$366.3^{+2.3(+20)}_{-2.3(-39)}$	$384.0^{+2.7(+16)}_{-2.6(-35)}$	$433.0^{+3.7(+14)}_{-3.7(-35)}$	$457.7^{+4.5(+12)}_{-4.4(-34)}$	$537^{+10(+11)}_{-10(-37)}$	$635^{+27(+9.8)}_{-26(-40.0)}$
$S(r_{500c})E(z)^{4/3*}$	$454.9^{+9.6(+46)}_{-9.4(-77)}$	$496.3^{+7.7(+49)}_{-7.6(-81)}$	$553.9^{+6.1(+52)}_{-6.1(-88)}$	$566.0^{+5.9(+50)}_{-5.9(-84)}$	$644.0^{+8.7(+51)}_{-8.6(-88)}$	$710.6^{+10.1(+49)}_{-9.9(-88)}$	$763^{+18(+41)}_{-18(-80)}$	$905^{+44(+32)}_{-42(-76)}$
$S'(0.15r_{500c})^\ddagger$	0.76	0.82	0.67	0.71	0.63	0.60	0.61	0.61
$S'(r_{2500c})^\ddagger$	0.61	0.64	0.68	0.63	0.65	0.65	0.59	0.59
$S'(r_{500c})^\ddagger$	0.30	0.23	0.37	0.34	0.46	0.59	0.44	0.41

Notes.

* Error-weighted average of the redshift evolution scaled entropy measurements of the grouped sample in units of keV cm^2 within the corresponding temperature bin. The first set of errors above and below the measurements represent the statistical uncertainty, and the errors presented within the parenthesis represent the systematic uncertainty (see Sect. 4 for the details of the accounted systematics).

† $S'(r) = \frac{d \log(S(r))}{d \log(r/r_{500c})}$, the slope of the error-weighted average entropy measurements as a function of dimensionless radius in logarithmic space, in units of $\log(\text{keV cm}^2)$.

same parameter space, the systematic uncertainty of the metallicity profile has a very large impact on the electron density measurements, which results in the entropy measurements having large systematic uncertainties. At higher temperatures, the systematic uncertainties of the electron density measurements become smaller due to the reduced line emission, and the less significant Fe-L complex increases the statistical uncertainties.

Furthermore, we find that the redshift scaled average entropy and the average temperature measurements of our sample at the three radii follow power-law relations within the uncertainties. To quantify the normalizations and the slopes of the relations, we fit a power-law model to the measurements of the form $S(r)E(z)^{4/3} = A(T/T_{\text{piv}})^B$ where the $S(r)$ term stands for entropy measured at three characteristic radii ($0.15r_{500c}$, r_{2500c} , and r_{500c}), the T term stands for the characteristic temperature ($T(r < r_{500c})$), T_{piv} term stands for the pivot temperature, and the A and B terms stand for the normalization and the slope of the relation respectively. For our galaxy group sample, we took a pivot value of $T_{\text{piv}} = 1.44$ keV and obtained the best-fit power-law models to the average measurements at the three radii as shown in Fig. 13. Furthermore, we noticed that the slope of the $S(r) - T$ relations seem to be changing around $T = 1.44$ keV such that the warm/higher-mass groups in our sample ($T = 1.44 - 2.68$ keV) are steeper than the $S(r) - T$ relations of the cool/lower-mass groups ($T = 0.73 - 1.44$ keV). To quantify the difference, we separately fit the average measurements of the warm and cool groups using the same relation, assuming pivot values of $T_{\text{piv}} = 1.79$ and 1.08 keV, respectively. Best-fit parameters of the $S(r) - T$ relation at three radii for all galaxy groups in our sample, along with the best-fit parameters for the warm, and cool groups, are listed in Table 3.

As a result of the fitting procedure, we find that for all galaxy groups ($T = 0.73 - 2.68$ keV), the slopes of the $S(r_{2500c}) - T(r < r_{500c})$ and $S(r_{500c}) - T(r < r_{500c})$ relations ($B = 0.70^{+0.07}_{-0.07}$ and $0.69^{+0.09}_{-0.09}$ respectively) are in very good agreement with each other whereas we find that the slope of the $S(0.15r_{500c}) - T(r < r_{500c})$ relation ($B = 0.86^{+0.06}_{-0.06}$) being slightly steeper. We also compare our relations with the self-similar predictions presented in Voit et al. (2005). We find that our best-fit normalizations of the $S(r) - T$ relations are $> 5\sigma$ larger than the self-similar predictions at all radii. This agrees well with the previous findings on the entropy excess in galaxy groups and indicates that

non-gravitational processes such as AGN feedback and radiative cooling are non-negligible and play an important role in shaping the entropy profiles of galaxy groups. Moreover, we compare the best-fit slopes of the $S(0.15r_{500c}) - T(r < r_{500c})$, $S(r_{2500c}) - T(r < r_{500c})$, $S(r_{500c}) - T(r < r_{500c})$ relations for all galaxy groups in our sample with the self-similar prediction ($B_{\text{self}} = 1$ at all radii) and find that our slopes are 2.3, 4.3, 3.4σ shallower than the self-similar slope.

Furthermore, we compare the best-fit $S(r) - T$ relations of the warm and cool groups and find that the slopes of the warm/higher-mass groups, $B = 0.98^{+0.10}_{-0.10}$, $0.87^{+0.11}_{-0.11}$ and $0.72^{+0.17}_{-0.17}$, are much steeper than the slopes of the cool/lower-mass groups, $B = 0.59^{+0.16}_{-0.16}$, $0.32^{+0.22}_{-0.22}$ and $0.56^{+0.28}_{-0.28}$ at $0.15r_{500c}$, r_{2500c} and r_{500c} respectively. We then compare our best-fit normalizations of the warm and cool groups with the self-similar predictions presented in (Voit et al. 2005) and find that the normalizations for warm and cool groups are $> 5\sigma$ larger than the self-similar predictions at all radii. Moreover, we also compare the slopes of the warm and cool groups with the self-similar prediction and find that the best-fit slopes of the warm/higher-mass groups, $B = 0.98^{+0.10}_{-0.10}$, $0.87^{+0.11}_{-0.11}$ and $0.72^{+0.17}_{-0.17}$, agree much better with the self-similar prediction ($B_{\text{self}} = 1$) compared to the slopes of the cool/lower-mass groups, $B = 0.59^{+0.16}_{-0.16}$, $0.32^{+0.22}_{-0.22}$ and $0.56^{+0.28}_{-0.28}$, at $0.15r_{500c}$, r_{2500c} , and r_{500c} respectively. This comparison suggests that even though the non-gravitational processes significantly increase the overall entropy levels of galaxy groups at all temperature/mass scales, they result in the slope of the $S(r) - T$ relation for cool/lower-mass groups deviating more from the self-similar prediction compared to the slope of the warm/higher-mass groups that live at a temperature/mass parameter space closer to clusters.

We note that the observed flattening for the cool groups can also be due to other reasons, such as the selection effects or relatively large systematic uncertainties. The X-ray selection probability of galaxy clusters and groups has a dependency on the emission profile of the cluster and group (Clerc et al. submitted). Therefore, for the most robust calibration of the $S(r) - T$ scaling relation, a selection function that takes entropy at given radii as input should be used, which is currently not implemented in our framework for galaxy groups. In the future, a better understanding of the temperature and metallicity profiles of galaxy groups, along with the use of a profile-dependent selection function for

Table 3: Best-fit parameters of the $S(r) - T$ relation.

Relation	A (keV cm ²)	B
All groups ($T = 0.73 - 2.68$ keV, $T_{\text{piv}} = 1.44$ keV)		
$S(0.15r_{500c}) - T(r < r_{500c})$	195^{+2}_{-2}	$0.86^{+0.06}_{-0.06}$
$S(r_{2500c}) - T(r < r_{500c})$	418^{+6}_{-7}	$0.70^{+0.07}_{-0.07}$
$S(r_{500c}) - T(r < r_{500c})$	618^{+16}_{-19}	$0.69^{+0.09}_{-0.09}$
Warm groups ($T = 1.44 - 2.68$ keV, $T_{\text{piv}} = 1.79$ keV)		
$S(0.15r_{500c}) - T(r < r_{500c})$	235^{+4}_{-4}	$0.98^{+0.10}_{-0.10}$
$S(r_{2500c}) - T(r < r_{500c})$	485^{+9}_{-10}	$0.87^{+0.11}_{-0.11}$
$S(r_{500c}) - T(r < r_{500c})$	717^{+24}_{-26}	$0.72^{+0.17}_{-0.17}$
Cool groups ($T = 0.73 - 1.44$ keV, $T_{\text{piv}} = 1.08$ keV)		
$S(0.15r_{500c}) - T(r < r_{500c})$	155^{+3}_{-4}	$0.59^{+0.16}_{-0.16}$
$S(r_{2500c}) - T(r < r_{500c})$	352^{+11}_{-13}	$0.32^{+0.22}_{-0.22}$
$S(r_{500c}) - T(r < r_{500c})$	504^{+21}_{-27}	$0.56^{+0.28}_{-0.28}$

Notes. The fitted relation is of the form $S(r)E(z)^{4/3} = A(T/T_{\text{piv}})^B$ where the $S(r)$ term stands for entropy measured at three characteristic radii ($0.15r_{500c}$, r_{2500c} , and r_{500c}), the T term stands for the characteristic temperature, $T(r < r_{500c})$, and T_{piv} is the pivot temperature value. The relation is fitted to the measurements presented in Table 2 by taking into account the statistical and systematic uncertainties. The fitting procedure is executed three times at each radius: first, for all the groups in the sample spanning a temperature range of 0.73 – 2.68 keV; second, for only the warm groups spanning a temperature range of 1.44 – 2.68 keV; and third, for only the cool groups spanning a temperature range of 0.73 – 1.44 keV.

fitting the $S(r) - T$ relation, would make the picture clearer and help us understand the origin of the observed flattening for the cool/lower-mass groups.

Comparing the entropy measurements at the three radii, with the previous measurements in the literature as a function of temperature, $T(r < r_{500c})$, is challenging given the limited number of studies reporting these quantities and the information provided in these studies to account for the discrepancies in the measurement radii being limited across the literature. In this section, we present our findings from the comparison performed between our measurements and the results reported by S09 and Johnson et al. (2009).

To have a fair comparison, we quantify and account for the systematic differences between our results and those presented in S09. The average temperature of galaxy groups in S09 are measured using core-excised apertures ($0.15r_{500c} < r < r_{500c}$), whereas in this work, we measure temperatures including the core out to r_{500c} to maximize the signal-to-noise in our measurements. We convert the core-excised characteristic temperature measurements, $T(0.15r_{500c} < r < r_{500c})$, reported in S09 to the core-included temperatures by applying a conversion factor of $T(r < r_{500c})/T(0.15r_{500c} < r < r_{500c}) = 1.07$. This conversion factor is obtained by projecting the average group temperature profile (see Sect. 4.1) using the temperature weighting and projection formulation of ZuHone et al. (2023) calibrated for eROSITA and the average group electron density profile (Bahar et al. in preparation). Additionally, we apply a correction factor to account for the difference in the characteristic radii estimation to the S09 entropies as described in Sect. 4.3. The correction

factors are obtained by comparing our scaling relations based on r_{500c} estimates with the masses obtained assuming hydrostatic equilibrium (see Sect. 4.1) and quantifying the impact of the mismatch on the average entropy measurements at three characteristic radii. Lastly, we apply a 5% correction to the entropy measurements of S09 to account for the 15% flux discrepancy between *Chandra* and eROSITA (see Sect. 4.2) that is reported in Bulbul et al. (submitted).

The comparison between our temperature and entropy measurements with the findings of S09 are shown in Fig. 14. After the systematic differences are accounted for, we find our measurements to agree well with the S09 results within $\sim 1\sigma$ confidence at all three radii. Fig. 14 shows that our results only deviate from the measurements of S09 at the cooler temperatures with $T(r < r_{500c}) < 1.15$ keV. We argue that this may be due to the completeness of our sample being much higher than the completeness of the S09 sample at these temperatures. The S09 sample is based on the archival *Chandra* follow-up observations of 43 ROSAT-detected bright groups. For this reason, by construction, the limited number of measurements reported in S09 at the low-temperature parameter space is for bright groups that have relatively high n_e and low S . This effect is visible in Fig. 14 such that S09 has only three measurements for $S(r_{500c})$ and 11 for $S(r_{2500c})$ and $S(0.15r_{500c})$ at the cool temperatures end, whereas our sample includes temperature measurements of a sample of 323 galaxy groups binned into 61 groups.

Furthermore, Johnson et al. (2009) analyzed XMM-Newton observations of 28 nearby galaxy groups and found that the entropy measurements of their sample at the core, $S(0.1r_{500c})$, follow a power-law relation with their core-excised temperature measurements, $T(0.1r_{500c} < r < 0.3r_{500c})$. They further report that the best-fit slope of their $S(0.1r_{500c}) - T(0.1r_{500c} < r < 0.3r_{500c})$ relation (0.79 ± 0.06) agrees with the slope of a similar relation, $S(0.15r_{500c}) - T(0.15r_{500c} < r < r_{2500c})$, presented in S09, 0.78 ± 0.12 . In our work, we measure entropy at the core at a slightly different radius ($0.15r_{500c}$) than the one used in Johnson et al. (2009), and we use core-included temperature measurements rather than the core-excised temperatures. Nevertheless, we compare our most similar relation, $S(0.15r_{500c}) - T(r < r_{500c})$, to the relations fitted in S09 and Johnson et al. (2009) and find that our slope 0.86 ± 0.08 is in good statistical agreement with the slopes of S09 and Johnson et al. (2009). Moreover, we further compare our best-fit slope for the $S(r_{2500c}) - T(r < r_{500c})$ relation with the best-fit slope of another similar relation, $S(r_{2500c}) - T(0.15r_{500c} < r < r_{500c})$, presented in S09 and find that our slope (0.7 ± 0.07) agrees well with the slope reported in S09 (0.76 ± 0.06). Lastly, we compare the best-fit slope of our $S(r_{500c}) - T(r < r_{500c})$ relation with the best-fit slope of S09 for the $S(r_{500c}) - T(0.15r_{500c} < r < r_{500c})$ relation and find that our slope (0.69 ± 0.9) is in good statistical agreement with the slope reported in S09 (0.8 ± 0.2).

6. Comparison with the Numerical Simulations

In this section, we compare our results with the state-of-the-art simulations to place constraints on the physics of the AGN feedback. We quantify the agreement or disagreement between our measurements and the predictions of the various AGN feedback models implemented in these cosmological hydrodynamical simulations, including MillenniumTNG¹⁰ (Hernández-Aguayo et al. 2023; Pakmor et al. 2023), Magneticum¹¹ (Hirschmann

¹⁰ <https://www.mtng-project.org>

¹¹ <http://www.magneticum.org>

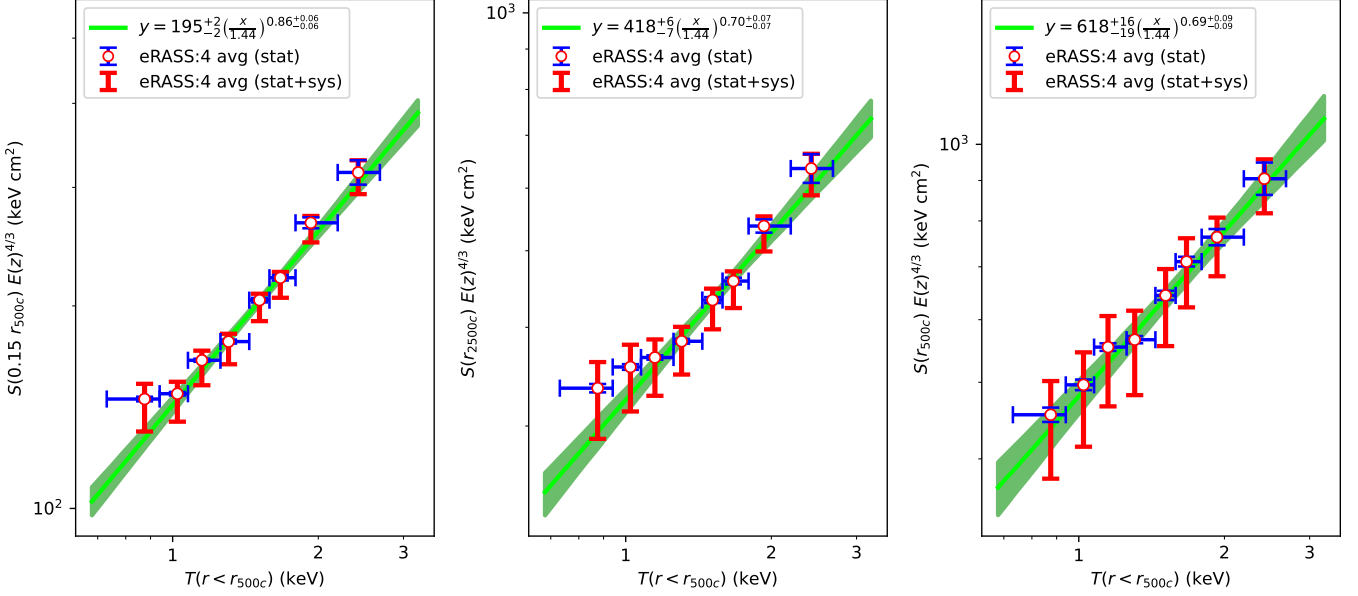


Fig. 13: $S(r) - T$ relations at $0.15r_{500c}$, r_{2500c} and r_{500c} . The white circles represent redshift evolution scaled average entropy measurements, blue error bars represent statistical uncertainties of the averages, and the red error bars represent the overall error budget of the average measurements resulting from the statistical and systematic uncertainties (see Sect. 4 for the details of the accounted systematics). The best-fit power-law models to the data points are plotted as light green lines, and the uncertainties of the best-fit lines are shown with dark green shaded regions.

et al. 2014) and the OverWhelmingly Large Simulations (OWL simulations, Schaye et al. 2010).

We compare our results with the Magneticum, MillenniumTNG, and OWL simulations that include different implementations for AGN feedback. The entropy measurements of the OWL simulations are plotted in Fig. 2 of McCarthy et al. (2010); therefore, we extracted their measurements from their paper and directly used them in this work. In contrast, the entropy and the characteristic temperature profile measurements for MillenniumTNG and Magneticum simulations are not publicly available. For this reason, we extract thermodynamic profiles of the gaseous halos from the MillenniumTNG and Magneticum simulations. A brief description of the MillenniumTNG and Magneticum simulations and the extraction process is as follows.

6.1. MillenniumTNG

The MTNG740 flagship full physics run of the MillenniumTNG project (Pakmor et al. 2023) is used in this work which simulates a 500 Mpc/h cosmological box with the Planck Collaboration et al. (2016) cosmology. Its galaxy formation model is close to the IllustrisTNG model (Weinberger et al. 2017; Pillepich et al. 2018) and includes primordial and metal line cooling, a subgrid model for star formation and the interstellar medium, mass return from stars via AGB stars and supernovae, an effective model for galactic winds, as well as a model for the formation, growth, and feedback from supermassive black holes. At a baryonic mass resolution of $3 \times 10^7 M_{\odot}$, MTNG740 reproduces well many properties of observed galaxies and galaxy clusters for halos with $M_{500c} > 2.3 \times 10^{12} M_{\odot}$.

The hydrodynamical profiles of groups shown in this work are computed the same way as the galaxy cluster profiles in Pakmor et al. (2023). MTNG outputs a number of useful quantities: gas cell mass (m), electron abundance (x), and internal

energy (ϵ). Assuming a primordial hydrogen mass fraction of $X_H = 0.76$, and an adiabatic index of $\gamma = 5/3$, we compute the volume-weighted electron number density, n_e , and temperature T , for each gas particle i as

$$V_i n_{e,i} = x_i m_i \frac{X_H}{m_p} \quad (11)$$

$$T_i = (\gamma - 1) \epsilon_i / k \frac{4m_p}{1 + 3X_H + 4X_H x_i}, \quad (12)$$

where m_p the proton mass and k is the Boltzmann constant. We then compute the averages of the two quantities in radial bins \hat{b}_j :

$$n_{e,j} = V^{-1}(\hat{b}_j) \sum_{i \in \hat{b}_j} V_i n_{e,i} \quad (13)$$

$$T_j = N^{-1}(\hat{b}_j) \sum_{i \in \hat{b}_j} T_i, \quad (14)$$

where $N(\hat{b}_j)$ is the number of gas cells in bin \hat{b}_j . The radial bins are chosen as 23 logarithmically spaced intervals between 0.001 and $10 r_{200c}$, where r_{200c} is the radius from the halo center encompassing 200 times the critical density of the Universe, ρ_c . As a derived quantity, we also compute the entropy as:

$$S(\hat{b}_j) = \frac{T(\hat{b}_j)}{n_e(\hat{b}_j)^{2/3}}. \quad (15)$$

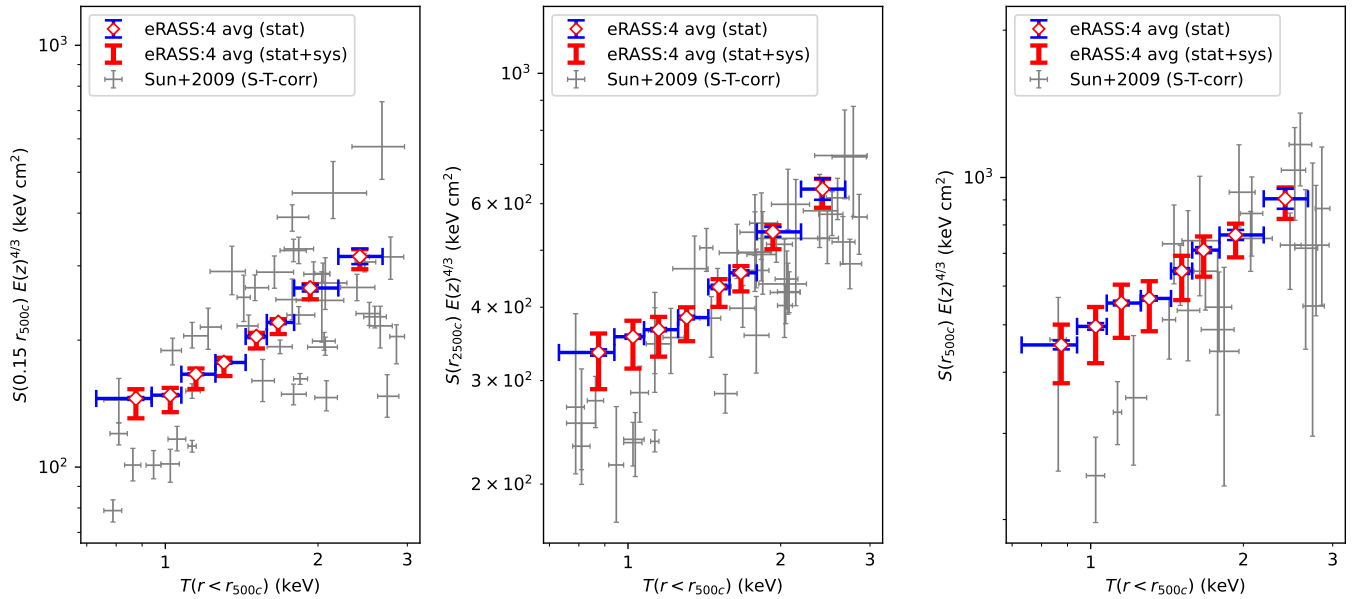


Fig. 14: Comparison between the redshift evolution scaled average eROSITA entropy measurements (white diamonds) with the *Chandra* measurements of 43 galaxy groups (black error bars) presented in S09 at three radii ($0.15r_{500c}$, r_{2500c} , r_{500c}) as a function of characteristic temperature, $T(r < r_{500c})$. Blue error bars represent the statistical uncertainties of the average measurements, and the red error bars represent the overall error budget resulting from the statistical and systematic uncertainties (see Sect. 4 for the details of the accounted systematics). For consistency, core-excised temperatures presented in S09 are converted to core-included temperatures, and the entropy measurements presented in S09 are normalized such that the new data points are measured at the same angular radii with eROSITA flux calibration (see Sect. 5 for the details of these corrections).

6.2. Magneticum Simulations

The Magneticum simulations used in this work were performed with the TreePM/SPH code P-Gadget3, an extended version of P-Gadget2 (Springel 2005). In addition to hydrodynamics and gravity, the simulations also account for a variety of physical baryonic processes, including radiative cooling and heating from a time-dependent UV background (Haardt & Madau 2001), star formation and feedback (Springel & Hernquist 2003), metal enrichment from stellar evolution (Tornatore et al. 2004, 2007), and black hole growth and gas accretion powering energy feedback from AGN (Springel et al. 2005; Di Matteo et al. 2005; Fabjan et al. 2010). In this study, we consider a sample of 22,254 galaxy groups and clusters with mass $M_{500c} > 5 \times 10^{12} M_{\odot}$ identified using the SubFind algorithm (Springel et al. 2001; Dolag et al. 2009) in the “Box2_hr” simulation box. This covers a comoving volume of $(352h^{-1}\text{cMpc})^3$ and is resolved with 2×1584^3 particles (which correspond to mass resolutions of $m_{\text{DM}} = 6.9 \times 10^8 h^{-1} M_{\odot}$ and $m_{\text{gas}} = 1.4 \times 10^8 h^{-1} M_{\odot}$, for DM and gas respectively). A Λ CDM cosmology with $h = 0.704$, $\Omega_b = 0.0451$, $\Omega_m = 0.272$, $\Omega_{\Lambda} = 0.728$ and $\sigma_8 = 0.809$ is employed (from the 7-year results of the Wilkinson Microwave Anisotropy Probe Komatsu et al. 2011). See also Biffi et al. (2022) for further details.

We compute gas thermodynamical profiles by selecting the hot, diffuse gas component in each halo of the sample, characterized by temperature higher than $5 \times 10^5 K$ and non-star-forming, representing the X-ray emitting intra cluster and group mediums. The gas mass-weighted temperature and electron density radial profiles are then generated by considering three-dimensional radial bins. The profiles of massive haloes are resolved with 50 linear radial bins up to $1.5 r_{500c}$. For smaller systems resolved with fewer gas particles, we instead adopt an equal-particle bin-

ning of the radial profiles, in order to ensure statistically reliable estimates. In all cases, we ensure a minimum of 150 selected gas particles in each radial shell.

6.3. Overwhelmingly Large Simulations

The Overwhelmingly Large Simulations (Schaye et al. 2010) used in this work is a cosmological hydrodynamical simulation that were performed using an extended version of the ThreePM/SPH code Gadget3 (Springel 2005). The simulations include radiative cooling (Wiersma et al. 2009a), star formation (Schaye & Dalla Vecchia 2008), stellar evolution and chemical enrichment (Wiersma et al. 2009b), kinetic supernovae feedback (Dalla Vecchia & Schaye 2008) and feedback from supermassive black holes (Springel et al. 2005; Booth & Schaye 2009). The simulations employ a flat Λ CDM cosmology with $h = 0.73$, $\Omega_b = 0.0418$, $\Omega_m = 0.238$, $\Omega_{\Lambda} = 0.762$ and $\sigma_8 = 0.74$ that are taken from the analysis of 3-year results of WMAP (Spergel et al. 2007). The entropy and temperature measurements of galaxy groups in OWL simulations are taken from McCarthy et al. (2010) where ~ 200 galaxy groups are selected by applying a mass criterion of $M_{200c} > 10^{13} M_{\odot}$. The temperature and electron density profiles are obtained by emission-weighting the gas properties, and the entropy measurements are obtained by combining the temperature and electron density measurements.

They ran their simulations two times. In their first run (AGN run), they included all the sub-grid physics listed above, and in their second run (REF run), they turned off the AGN feedback. Both runs are indistinguishable in all aspects, with the only difference being that the former includes feedback from supermassive black holes as prescribed in (Booth & Schaye 2009). We refer the reader to Schaye et al. (2010) and McCarthy et al.

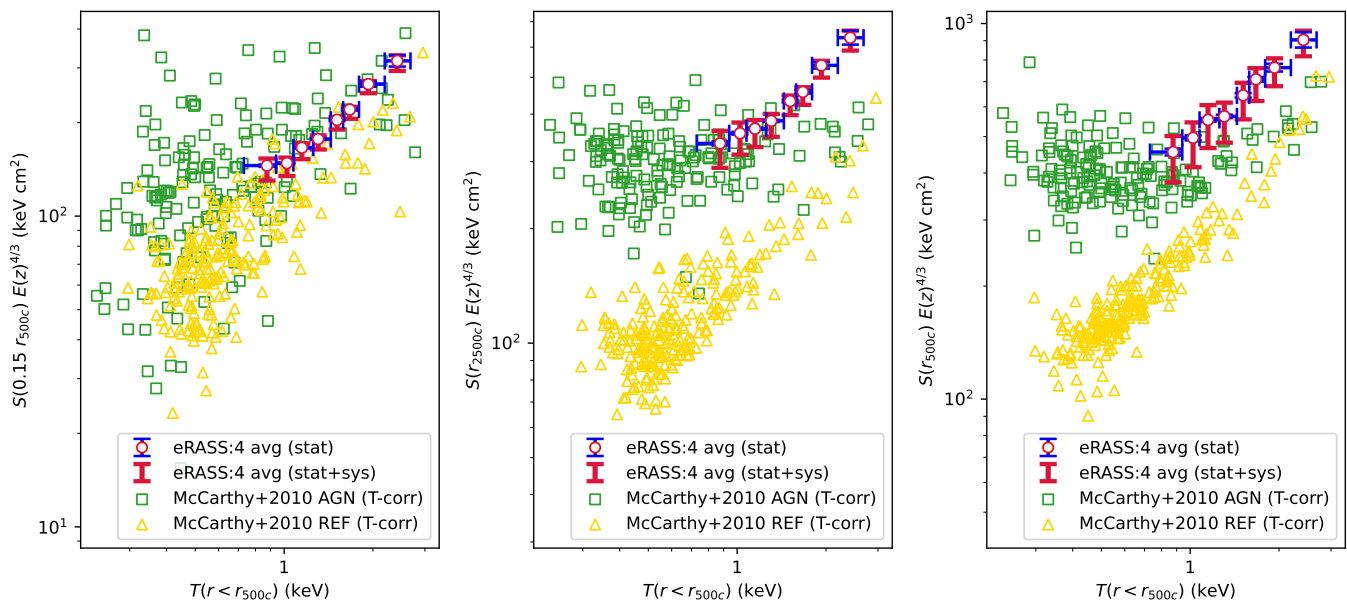


Fig. 15: Comparison between the redshift evolution scaled average eROSITA entropy measurements (white circles) with the predictions of the REF (AGN feedback off) and AGN (AGN feedback on) runs of OWL simulations (yellow triangles and green squares) presented in McCarthy et al. (2010) at three radii ($0.15r_{500c}$, r_{2500c} , r_{500c}) as a function of characteristic temperature, $T(r < r_{500c})$. Blue error bars represent the statistical uncertainties of the average measurements, and the red error bars represent the overall error budget resulting from the statistical and systematic uncertainties (see Sect. 4 for the details of the accounted systematics). For consistency, core-excised temperatures presented in McCarthy et al. (2010) are converted to core-included temperatures (see Sect. 6 for the details of the correction).

(2010) for further details on the OWL simulations and the measurements of the thermodynamic properties of the galaxy groups in OWLS.

6.4. Comparisons of Observations with OWL, MillenniumTNG and Magneticum Simulations

A fair comparison between simulations and observations is only possible when the compared samples are subject to a similar selection and the simulated temperatures are weighted with a well-calibrated temperature weighting scheme that would reproduce the observed spectroscopic-like temperatures. We achieve this by using the eROSITA selection function that is obtained by applying the same cleaning procedure described in Sect. 2 to the mock catalogs from the eROSITA’s digital twin (Seppi et al. 2022). The eRASS1 selection function, encapsulating the selection and cleaning information, provides detection probabilities of the group- and cluster-scale dark matter haloes as a function of M_{500c} and z (see Clerc et al. submitted, for details). The selection function obtained through this procedure is applied to the MillenniumTNG and Magneticum clusters and groups, and the entropy profiles of the simulated samples are measured at the three characteristic radii. Furthermore, the spectroscopic-like characteristic temperatures, $T(r < r_{500c})$, are obtained by weighting and projecting the simulated 3D temperature profiles of MillenniumTNG and Magneticum haloes, using the temperature weighting scheme calibrated for eROSITA (ZuHone et al. 2023). Lastly, we compare the entropy and characteristic temperature measurements of simulated groups with the observations.

Before comparing our results with the simulations employing different AGN feedback implementations, we first test the reference (REF) run of the OWL simulations of McCarthy et al.

(2010) with the observations. The predictions of the REF run serve as a baseline simulation and can be used to test the overall impact of the AGN feedback on the entropy profiles and characteristic temperatures of groups (Schaye et al. 2010). Their REF run is performed with their full model, identical to their final run, but does not include AGN feedback. To have a fair comparison, we convert the core-excised characteristic temperature measurements in simulations ($T(0.15r_{500c} < r < r_{500c})$) to the core-included temperatures, $T(r < r_{500c})$, following the same approach presented in Sect. 5. After the correction, we compare our measurements and the predictions of the REF run of the OWL simulations at the three characteristic radii, as shown in Fig. 15. We find that the main visible effect of AGN feedback is to lift the entropy values of the groups outside the core (e.g., at r_{2500c} or r_{500c}) for all groups, with a more marked effect at the lowest temperatures. The excess entropy induced by the AGN feedback in observations leads to significant disagreement between our measurements and the predictions of their REF run outside the core. On the other hand, the consistency with the AGN run (the twin simulations of the REF run, but the AGN feedback is turned on) suggests that the observations significantly favor the presence of strong AGN feedback in galaxy groups. It can further be seen from Fig. 15 that at the core $0.15r_{500c}$, the data points of McCarthy et al. (2010) for the AGN feedback run are indistinguishable from data points of the reference run, and their results agree well with ours at this radius. Contrarily, outside the core (at r_{2500c} or r_{500c}), the reference and the feedback runs are significantly different at the low-temperature parameter space, indicating the strong AGN feedback imprint. This suggests that the entropy measurements at the core probe the AGN feedback much less efficiently than those outside the core at the group scale haloes, which is also shown in McCarthy et al. (2010) for core-excised quantities. We note that the agreement at the core

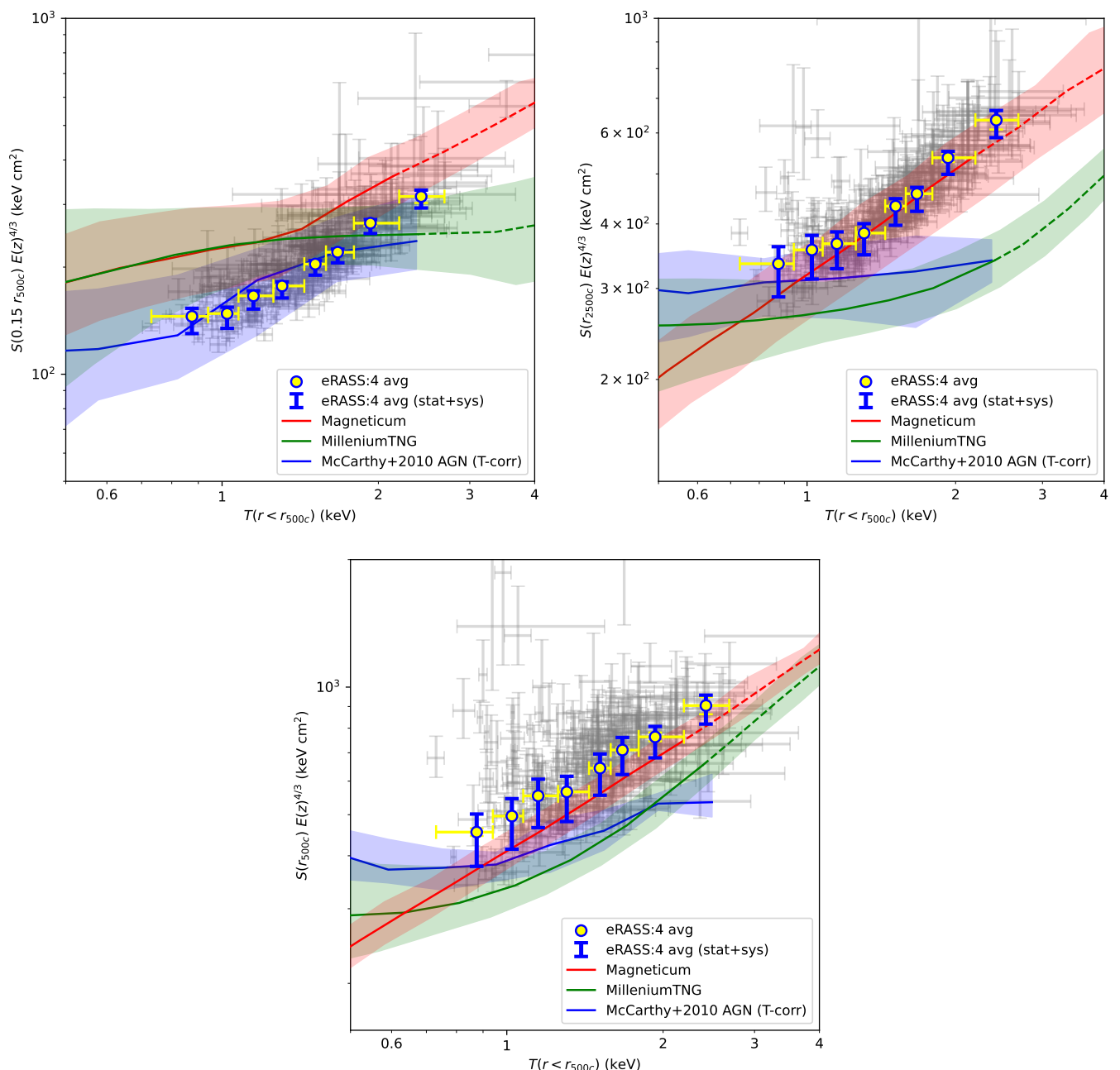


Fig. 16: Comparison of the redshift evolution scaled average eROSITA entropy measurements (yellow circles) with the predictions of three simulations (Magneticum, MillenniumTNG, and OWL simulations) at $0.15r_{500c}$ (top left), r_{2500c} (top right) and r_{500c} (bottom) as a function of characteristic temperature, $T(r < r_{500c})$. Gray crosses represent the average entropy measurements of the binned groups, and the blue error bars represent the overall error budget of the average measurements resulting from the statistical and systematic uncertainties (see Sect. 4 for the details of the accounted systematics). The solid lines represent the predictions of simulations at the group regime ($5 \times 10^{12} < M_{500c} < 10^{14} M_{\odot}$), the dashed lines represent the predictions at the low-mass cluster regime ($10^{14} < M_{500c} < 3 \times 10^{14} M_{\odot}$) and the shaded regions represent the scatter of the measurements.

of groups between the reference and AGN feedback runs are obtained from the OWL simulations, where a thermal AGN feedback model is implemented. It is unclear whether such a conclusion would hold true for simulations implementing a feedback model that includes both kinetic and thermal feedback that leads to significant turbulent stirring in the core, such as MillenniumTNG. Therefore, to verify the universality of the conclusion, further tests are required to be conducted in the future on simulations implementing kinetic and thermal feedback.

After comparing our measurements with the (REF) run of the OWL simulations, we compare our results with the three simulations employing different AGN feedback implementations: Magneticum, MillenniumTNG, and OWL (AGN run). The comparison between our measurements and the predictions of the simulations at the three characteristic radii is shown in Fig. 16.

At the cores of groups ($0.15r_{500c}$), we find the eROSITA observations agreeing relatively well with the OWL simulations between the IGrM temperatures $T = 0.73 - 1.79$ keV whereas at the

warmer IGrM temperatures $T = 1.79\text{--}2.68$ keV the observations fall above their predictions. We further find that the Magneticum and MillenniumTNG simulations overpredict the average entropy for the cool/lower-mass groups ($T = 0.73 - 1.44$ keV), whereas the agreement becomes better in the MillenniumTNG at the warmer IGrM temperatures, close to the cluster ICM temperature range. Even though our measurements disagree with the average entropy predictions of Magneticum and MillenniumTNG, our measurements still lie within the 1σ scatter of the simulated profiles.

At the mid-region of groups (r_{2500c}), the entropy measured by eROSITA agrees well with the Magneticum and OWL simulation for cool/lower-mass groups, whereas the MillenniumTNG simulations underpredict the entropy for the groups in this region at a $\sim 2.5\sigma$ level. We find that our measurements also agree well with the Magneticum simulations for warm/higher-mass groups. Furthermore, we find that as the temperatures/masses of the groups increase ($T > 1.44$ keV) and approach the cluster temperatures/masses, the offset between observations and the predictions of MillenniumTNG and OWL simulations becomes more significant, starting from a statistical disagreement level of 3.5σ at $T = 1.44$ keV and going up to a level of 8.5σ at $T = 2.68$ keV.

At the group outskirts (r_{500c}), we observe an overall agreement between the eROSITA observations and the Magneticum simulations at all temperatures. While the entropy measurements of galaxy groups in MillenniumTNG simulations are slightly below observations, we find that they are consistent at a 2σ confidence level at all temperatures. Although our measurements are in 1σ agreement with the OWL simulations for cooler/lower-mass groups $T < 1.44$ keV, the departure from observations becomes more significant ($> 2\sigma$) at warmer temperatures, close to the ICM regime.

The AGN feedback implementations in most large-scale simulations are variations of the (Springel et al. 2005; Di Matteo et al. 2005) model. Even though similar in spirit, different adaptations and extensions to the original model have been made for the different simulations, leading to a strongly varying impact on the hot gas among the three simulations covered in this work. While the main feature behind the model for the OWL simulation is to achieve an effective AGN feedback by accumulating the injected energy until a ΔT_{heat} is reached, Magneticum and MillenniumTNG introduce a transition from quasar-mode to a stronger radio mode feedback (e.g. see Sijacki et al. 2007; Fabjan et al. 2010) instead. However, while in Magneticum the radio mode feedback is still modeled as a isotropic, thermal feedback with an increased efficiency (e.g. see Hirschmann et al. 2014), in MillenniumTNG it is modeled as a kinetic feedback (e.g. see Pillepich et al. 2018; Weinberger et al. 2017). In addition to these differences, the detailed setting within the individual models can not only significantly change the distribution and properties of gas within galaxies, but also impact the hot gas and especially the entropy within and around clusters and groups (e.g. see figure 3 in Fabjan et al. 2010). Subsequently, in an updated version of the OWL simulations (Le Brun et al. 2014), three different ΔT_{heat} parameters (10^8 , $10^{8.5}$ and $10^{8.7}$ keV) of the Booth & Schaye (2009) model, coupled with the burstiness and the energeticness of the feedback, are tested. The authors report that ΔT_{heat} can be used to tune the impact of the feedback in the IGrM gas. They further show that for groups, the normalization and slope of the $S - T$ relation (or the $S - M$ relation) does not depend much on ΔT_{heat} at the core ($0.15r_{500c}$). In comparison, an increase in the ΔT_{heat} parameter corresponds to a larger normalization and possibly a different slope at the outskirts (r_{2500c} and r_{500c}) due to

the low-entropy gas getting ejected (see Fig. 6 in Le Brun et al. 2014). This can also be seen in Fig. 7 of Le Brun et al. (2014) where the gas gets ejected in the case of more bursty and energetic feedback and results in lower densities at all radii out to $1.6r_{500c}$.

In light of these indications found within simulations, the discrepancy between the observed entropy and the predictions of MillenniumTNG and OWL simulations at the outskirts can be justified by the effectiveness and energetics of the individual AGN feedback models being not sufficient to match our observations at the group scale. The weaker AGN feedback found in MillenniumTNG, leading to lower entropy in the outskirts, may also be related to the elimination of the magnetic fields from the TNG physics model, as noted in Pakmor et al. (2023). The agreement between the observations and the Magneticum simulations in the group outskirts suggest that the underlying model is able to effectively treat a broad range in mass, extending the previously reported good agreement of entropy profiles for galaxy clusters (Planelles et al. 2014; Rasia et al. 2015) to group scales.

The agreement between the entropy measurements in eROSITA observations and the numerical simulations at the cores is better than the outskirts. Slightly higher entropy in simulations is harder to explain using the Booth & Schaye (2009) model since the normalization and the shape at the core ($0.15r_{500c}$) do not seem to be affected by the change of the ΔT_{heat} parameter in the runs presented in Le Brun et al. (2014).

We note that the interpretations above for the OWL simulation assume that the Booth & Schaye (2009) model can reproduce the gas properties by tuning the ΔT_{heat} parameter relatively accurately, which may or may not be the case. Furthermore, as also discussed above, the AGN feedback implementation in MillenniumTNG and Magneticum simulations are even different (among them as well as compared to OWL). For these reasons, a more detailed analysis would be needed to understand better which aspects of the underlying AGN feedback models are driving the differences between the simulations and the eROSITA observations, which is beyond the scope of this paper. Furthermore, we note that the selection function we used in this work is a function of mass and redshift, and the use of it significantly improves the robustness of our comparison. In future studies, a profile-dependent selection function can be used that would make the selection procedure applied to the simulations even more realistic. Ultimately, the most accurate comparison would be achieved by producing synthetic eROSITA observations through fully forward modeling cosmological hydrodynamic simulations to which the same detection and data analysis pipeline used for real observations can be applied.

7. Conclusions

Our work places the tightest constraints on the impact of AGN feedback on the average thermodynamic properties by populating the low mass galaxy groups down to cool IGrM temperatures of 0.7 keV. eROSITA's superb sensitivity in the soft X-ray band lead to the detection of a large number of galaxy groups with a well-understood selection function. When stacked, the eROSITA data provides unprecedented statistical power for the measurements of X-ray properties of these sources. We use a sample of 1178 galaxy groups to place constraints on the impact of AGN feedback on the thermodynamic properties of the IGrM. We select the galaxy group sample based on the primary sample of the eRASS1 clusters and groups and apply a rigorous selection and cleaning. The cleaning procedure is designed to provide a pure sample with a well-defined selection function while maximiz-

ing the sample size. A Bayesian imaging analysis is carried out for all the 1178 galaxy groups in the sample where the nearby clusters and bright point sources are co-fit. The galaxy groups with similar statistical and physical properties, such as count and temperature, are then grouped together into 271 bins. A joint Bayesian spectral fitting is performed on the groups in the same bin to increase the statistical power in each bin with the sources with similar properties.

Constraining baryonic physics at group scales is a highly challenging task. Systematic effects must be considered to achieve a reliable and robust conclusion. We quantify and discuss three major systematics for thermodynamic profile studies and conservatively take them into account for our final measurements and conclusions. Besides the robust thermodynamic property measurements, we also provide a detailed comparison of our findings with the state-of-the-art simulations by accounting for the selection effects. We assess the agreement between our measurements and the simulations employing various AGN feedback implementations to pave the way for a more realistic AGN feedback modeling in numerical simulations.

This paper is the first in-depth study of galaxy groups with eROSITA focusing on the impact of AGN feedback on the entropy and temperature measurements within an overdensity radius. The main conclusions of this work are as follows:

- With a sample of 1178 galaxy groups and average thermodynamic properties of 271 binned groups, our work stands as the most comprehensive study of the hot gas in galaxy groups in terms of sample size, diversity, and statistics. The selection effects are considered for the first time while comparing the measured thermodynamic profiles of galaxy groups with the numerical simulations.
- Overall, the entropy measurements at three characteristic radii: $0.15r_{500c}$, r_{2500c} and r_{500c} and the characteristic temperature of the galaxy groups detected in the eROSITA first All-Sky Survey observations are in good agreement with the previously reported results in S09 and Johnson et al. (2009) within the uncertainties (see Sect. 4). The largest mismatch between the eROSITA measurements presented in this work and the *Chandra* measurements presented in S09 is at the low-temperature parameter space ($T(r < r_{500c}) < 1.15$ keV). We argue that this is because the completeness and the selection of the two samples being different in this temperature range. The archival sample used in S09 consists mostly of bright galaxy groups detected in *ROSAT* observations and followed up by *Chandra*. In contrast, the group sample used in this work has a more uniform and well-defined selection.
- We compare our entropy measurements with the reference (REF) run of OWL simulations that include various non-gravitational processes except the AGN feedback. From this comparison, we conclude that the impact of AGN feedback on the entropy profiles of groups is significant at the outskirts (r_{2500c} and r_{500c}), and less pronounced near the core ($0.15r_{500c}$). This result suggests that for groups, AGN feedback has a larger impact on the outskirts than the core, contrary to its impact on the observed gas properties of clusters of galaxies (Le Brun et al. 2014). Due to their shallower potential wells, the feedback from the central black hole is able to move the low entropy gas to much further radii to the outskirts in galaxy groups.
- Our measurements have significant constraining power on the impact of AGN feedback on the thermodynamic properties of the IGrM gas and serve as a reference for the feedback implementations in numerical simulations and theoret-

ical models. We compare our results with three state-of-the-art cosmological hydrodynamic simulations, including MillenniumTNG, Magneticum, and OWL, employing various AGN feedback implementations by accounting for the selection effects. In the cores of the galaxy groups, the entropy agrees well with OWL simulations out to $T = 1.79$ keV. Although the sample averaged entropy from the MillenniumTNG and Magneticum simulations are higher, the measurements within the scatter of the respective simulations. At the outskirts, (r_{2500c} and r_{500c}), the observed entropy agrees well with the Magneticum simulations for groups with IGrM temperatures down to 0.79 keV. In OWL simulations, although we see a similar entropy flattening trend for the cooler groups, the departure from observations becomes significant towards the galaxy cluster regime at higher temperatures. A similar trend is observed in MillenniumTNG simulations; however, in this case, the entropy offset is relatively significant for all temperature regimes. Overall, the AGN feedback implementation in Magneticum simulations reproduces our observations the best at the three characteristic radii.

This work demonstrates the potential of eROSITA for exploring the baryonic physics at the galaxy groups out to large radii. Deeper data with the eROSITA All-sky Survey survey will allow the detection of a larger sample of galaxy groups pushing down in mass and IGrM temperature floors. Employing these groups in similar future studies with larger statistical power will enable to test hydrodynamical simulations in very cool temperatures below < 0.5 keV, which is currently unreachable with the eRASS1 sample.

Acknowledgements. This work is based on data from eROSITA, the soft X-ray instrument aboard SRG, a joint Russian-German science mission supported by the Russian Space Agency (Roskosmos), in the interests of the Russian Academy of Sciences represented by its Space Research Institute (IKI), and the Deutsches Zentrum für Luft und Raumfahrt (DLR). The SRG spacecraft was built by Lavochkin Association (NPOL) and its subcontractors and is operated by NPOL with support from the Max Planck Institute for Extraterrestrial Physics (MPE). The development and construction of the eROSITA X-ray instrument were led by MPE, with contributions from the Dr. Karl Remeis Observatory Bamberg & ECAP (FAU Erlangen-Nuernberg), the University of Hamburg Observatory, the Leibniz Institute for Astrophysics Potsdam (AIP), and the Institute for Astronomy and Astrophysics of the University of Tübingen, with the support of DLR and the Max Planck Society. The Argelander Institute for Astronomy of the University of Bonn and the Ludwig Maximilians Universität Munich also participated in the science preparation for eROSITA.

The eROSITA data shown here were processed using the eSASS/NRTA software system developed by the German eROSITA consortium.

E. Bulbul, A. Liu, V. Ghirardini, C. Garrel, S. Zelmer, and X. Zhang acknowledge financial support from the European Research Council (ERC) Consolidator Grant under the European Union’s Horizon 2020 research and innovation program (grant agreement CoG DarkQuest No 101002585). N. Clerc was financially supported by CNES. S. Bose is supported by the UK Research and Innovation (UKRI) Future Leaders Fellowship [grant number MR/V023381/1]. C. Hernández-Aguayo acknowledges support from the Excellence Cluster ORIGINS which is funded by the Deutsche Forschungsgemeinschaft (DFG, German Research Foundation) under Germany’s Excellence Strategy – EXC-2094 – 390783311.

This work made use of the following Python software packages: Astropy¹² (Astropy Collaboration et al. 2022), Colossus¹³ (Diemer 2018), emcee¹⁴ (Foreman-Mackey et al. 2013), Matplotlib¹⁵ (Hunter 2007), NumPy¹⁶ (Harris et al. 2020),

¹² <https://www.astropy.org/>

¹³ <https://bdiemer.bitbucket.io/colossus/>

¹⁴ <https://emcee.readthedocs.io/>

¹⁵ <https://matplotlib.org/>

¹⁶ <https://numpy.org/>

pyfftw¹⁷ (Frigo & Johnson 2005) PyXspec¹⁸ (Arnaud 1996), SciPy¹⁹ (Virtanen et al. 2020), Vorbin²⁰ (Cappellari & Copin 2003),

References

- Arnaud, K. A. 1996, in *Astronomical Society of the Pacific Conference Series*, Vol. 101, *Astronomical Data Analysis Software and Systems V*, ed. G. H. Jacoby & J. Barnes, 17
- Asplund, M., Grevesse, N., Sauval, A. J., & Scott, P. 2009, *ARA&A*, 47, 481
- Astropy Collaboration, Price-Whelan, A. M., Lim, P. L., et al. 2022, *ApJ*, 935, 167
- Bahar, Y. E., Bulbul, E., Clerc, N., et al. 2022, *A&A*, 661, A7
- Balogh, M. L., Pearce, F. R., Bower, R. G., & Kay, S. T. 2001, *MNRAS*, 326, 1228
- Biffi, V., Dolag, K., Reiprich, T. H., et al. 2022, *A&A*, 661, A17
- Booth, C. M. & Schaye, J. 2009, *MNRAS*, 398, 53
- Brunner, H., Liu, T., Lamer, G., et al. 2022, *A&A*, 661, A1
- Bryan, G. L. 2000, *ApJ*, 544, L1
- Bulbul, E., Kraft, R., Nulsen, P., et al. 2020, *ApJ*, 891, 13
- Bulbul, E., Liu, A., Pasini, T., et al. 2022, *A&A*, 661, A10
- Bulbul, E., Markevitch, M., Foster, A., et al. 2014, *ApJ*, 789, 13
- Bulbul, E., X., .., & et al. submitted
- Bulbul, G. E., Hasler, N., Bonamente, M., & Joy, M. 2010, *ApJ*, 720, 1038
- Bulbul, G. E., Smith, R. K., Foster, A., et al. 2012, *ApJ*, 747, 32
- Buote, D. A. 2000, *ApJ*, 539, 172
- Buote, D. A. & Fabian, A. C. 1998, *MNRAS*, 296, 977
- Cappellari, M. & Copin, Y. 2003, *MNRAS*, 342, 345
- Cappelluti, N., Li, Y., Ricarte, A., et al. 2017, *ApJ*, 837, 19
- Cash, W. 1979, *ApJ*, 228, 939
- Chiu, I. N., Ghirardini, V., Liu, A., et al. 2022, *A&A*, 661, A11
- Clerc, N., X., .., & et al. submitted
- Comparat, J., Eckert, D., Finoguenov, A., et al. 2020, *The Open Journal of Astrophysics*, 3, 13
- Comparat, J., Merloni, A., Salvato, M., et al. 2019, *MNRAS*, 487, 2005
- Costanzi, M., Rozo, E., Rykoff, E. S., et al. 2019, *MNRAS*, 482, 490
- Coutinho, D., Ramos-Ceja, M. E., Dennerl, K., et al. 2022, in *Society of Photo-Optical Instrumentation Engineers (SPIE) Conference Series*, Vol. 12181, *Society of Photo-Optical Instrumentation Engineers (SPIE) Conference Series*, ed. J.-W. A. den Herder, S. Nikzad, & K. Nakazawa, 121811A
- Crain, R. A., Theuns, T., Dalla Vecchia, C., et al. 2009, *MNRAS*, 399, 1773
- Dalla Vecchia, C. & Schaye, J. 2008, *MNRAS*, 387, 1431
- Di Matteo, T., Springel, V., & Hernquist, L. 2005, *Nature*, 433, 604
- Diemer, B. 2018, *ApJS*, 239, 35
- Dolag, K., Borgani, S., Murante, G., & Springel, V. 2009, *MNRAS*, 399, 497
- Eckert, D., Gaspari, M., Gastaldello, F., Le Brun, A. M. C., & O’Sullivan, E. 2021, *Universe*, 7, 142
- Fabjan, D., Borgani, S., Tornatore, L., et al. 2010, *MNRAS*, 401, 1670
- Finoguenov, A., Jones, C., Böhringer, H., & Ponman, T. J. 2002, *ApJ*, 578, 74
- Foreman-Mackey, D., Hogg, D. W., Lang, D., & Goodman, J. 2013, *PASP*, 125, 306
- Freyberg, M., Perinati, E., Pacaud, F., et al. 2020, in *Society of Photo-Optical Instrumentation Engineers (SPIE) Conference Series*, Vol. 11444, *Space Telescopes and Instrumentation 2020: Ultraviolet to Gamma Ray*, ed. J.-W. A. den Herder, S. Nikzad, & K. Nakazawa, 1144410
- Frigo, M. & Johnson, S. G. 2005, *Proceedings of the IEEE*, 93, 216, special issue on “Program Generation, Optimization, and Platform Adaptation”
- Gastaldello, F., Simionescu, A., Mernier, F., et al. 2021, *Universe*, 7, 208
- Ghirardini, V., Bulbul, E., Hoang, D. N., et al. 2021, *A&A*, 647, A4
- Ghirardini, V., Eckert, D., Etori, S., et al. 2019, *A&A*, 621, A41
- Goodman, J. & Weare, J. 2010, *Communications in Applied Mathematics and Computational Science*, 5, 65
- Gozaliasl, G., Finoguenov, A., Tanaka, M., et al. 2022, *VizieR Online Data Catalog*, J/MNRAS/483/3545
- Grandis, S., Mohr, J. J., Costanzi, M., et al. 2021, *MNRAS*, 504, 1253
- Haardt, F. & Madau, P. 2001, in *Clusters of Galaxies and the High Redshift Universe Observed in X-rays*, ed. D. M. Neumann & J. T. V. Tran, 64
- Harris, C. R., Millman, K. J., van der Walt, S. J., et al. 2020, *Nature*, 585, 357
- Henley, D. B. & Shelton, R. L. 2013, *ApJ*, 773, 92
- Hernández-Aguayo, C., Springel, V., Pakmor, R., et al. 2023, *MNRAS*, 524, 2556
- HI4PI Collaboration, Ben Bekhti, N., Flöer, L., et al. 2016, *A&A*, 594, A116
- Hickson, P. 1982, *ApJ*, 255, 382
- Hickson, P. 1997, *ARA&A*, 35, 357
- Hirschmann, M., Dolag, K., Saro, A., et al. 2014, *MNRAS*, 442, 2304
- Humphrey, P. J., Buote, D. A., Brighenti, F., et al. 2012, *ApJ*, 748, 11
- Hunter, J. D. 2007, *Computing in Science & Engineering*, 9, 90
- Ider Chitham, J., Comparat, J., Finoguenov, A., et al. 2020, *MNRAS*, 499, 4768
- Johnson, R., Ponman, T. J., & Finoguenov, A. 2009, *MNRAS*, 395, 1287
- Kaastra, J. S. 2017, *A&A*, 605, A51
- Kluge, M., X., .., & et al. submitted
- Komatsu, E., Smith, K. M., Dunkley, J., et al. 2011, *ApJS*, 192, 18
- Le Brun, A. M. C., McCarthy, I. G., Schaye, J., & Ponman, T. J. 2014, *MNRAS*, 441, 1270
- Liu, A., Bulbul, E., Ghirardini, V., et al. 2022, *A&A*, 661, A2
- Lloyd-Davies, E. J., Ponman, T. J., & Cannon, D. B. 2000, *MNRAS*, 315, 689
- Lovisari, L., Etori, S., Gaspari, M., & Giles, P. A. 2021, *Universe*, 7, 139
- Lovisari, L. & Reiprich, T. H. 2019, *MNRAS*, 483, 540
- Lovisari, L., Reiprich, T. H., & Schellenberger, G. 2015, *A&A*, 573, A118
- Mazzotta, P., Rasia, E., Moscardini, L., & Tormen, G. 2004, *MNRAS*, 354, 10
- McCarthy, I. G., Schaye, J., Ponman, T. J., et al. 2010, *MNRAS*, 406, 822
- McDonald, M., Benson, B. A., Vikhlinin, A., et al. 2014, *ApJ*, 794, 67
- Merloni, A., X., .., & et al. 2024, *A&A*, 682, A34
- Mernier, F., de Plaa, J., Kaastra, J. S., et al. 2017, *A&A*, 603, A80
- Mernier, F., de Plaa, J., Werner, N., et al. 2018, *MNRAS*, 478, L116
- Mernier, F., Werner, N., Su, Y., et al. 2022, *MNRAS*, 511, 3159
- Migkas, K., X., .., & et al. submitted
- Mulchaey, J. S. 2000, in *Astronomical Society of the Pacific Conference Series*, Vol. 209, *IAU Colloq. 174: Small Galaxy Groups*, ed. M. J. Valtonen & C. Flynn, 174
- Mulchaey, J. S. & Zabludoff, A. I. 1998, *ApJ*, 496, 73
- Myles, J., Gruen, D., Mantz, A. B., et al. 2021, *MNRAS*, 505, 33
- Nagai, D., Kravtsov, A. V., & Vikhlinin, A. 2007, *ApJ*, 668, 1
- Pakmor, R., Springel, V., Coles, J. P., et al. 2023, *MNRAS*, 524, 2539
- Panagoulia, E. K., Fabian, A. C., & Sanders, J. S. 2014, *MNRAS*, 438, 2341
- Pillepich, A., Springel, V., Nelson, D., et al. 2018, *MNRAS*, 473, 4077
- Planck Collaboration, Ade, P. A. R., Aghanim, N., et al. 2016, *A&A*, 594, A13
- Planelles, S., Borgani, S., Fabjan, D., et al. 2014, *MNRAS*, 438, 195
- Ponman, T. J., Cannon, D. B., & Navarro, J. F. 1999, *Nature*, 397, 135
- Ponman, T. J., Sanderson, A. J. R., & Finoguenov, A. 2003, *MNRAS*, 343, 331
- Ponti, G., Zheng, X., Locatelli, N., et al. 2023, *A&A*, 674, A195
- Pratt, G. W., Arnaud, M., Piffaretti, R., et al. 2010, *A&A*, 511, A85
- Predehl, P., Andritschke, R., Arefiev, V., et al. 2021, *A&A*, 647, A1
- Rasia, E., Borgani, S., Murante, G., et al. 2015, *ApJ*, 813, L17
- Robotham, A. S. G., Norberg, P., Driver, S. P., et al. 2011, *MNRAS*, 416, 2640
- Rykoff, E. S., Rozo, E., Busha, M. T., et al. 2014, *ApJ*, 785, 104
- Rykoff, E. S., Rozo, E., Hollowood, D., et al. 2016, *ApJS*, 224, 1
- Sanders, J. S., X., .., & et al. in prep.
- Schaye, J. & Dalla Vecchia, C. 2008, *MNRAS*, 383, 1210
- Schaye, J., Dalla Vecchia, C., Booth, C. M., et al. 2010, *MNRAS*, 402, 1536
- Seppi, R., Comparat, J., Bulbul, E., et al. 2022, *A&A*, 665, A78
- Sijacki, D., Springel, V., Di Matteo, T., & Hernquist, L. 2007, *MNRAS*, 380, 877
- Simionescu, A., Werner, N., Mantz, A., Allen, S. W., & Urban, O. 2017, *MNRAS*, 469, 1476
- Smith, R. K., Brickhouse, N. S., Liedahl, D. A., & Raymond, J. C. 2001, *ApJ*, 556, L91
- Spergel, D. N., Bean, R., Doré, O., et al. 2007, *ApJS*, 170, 377
- Springel, V. 2005, *MNRAS*, 364, 1105
- Springel, V., Di Matteo, T., & Hernquist, L. 2005, *MNRAS*, 361, 776
- Springel, V. & Hernquist, L. 2003, *MNRAS*, 339, 289
- Springel, V., White, S. D. M., Tormen, G., & Kauffmann, G. 2001, *MNRAS*, 328, 726
- Sun, M. 2012, *New Journal of Physics*, 14, 045004
- Sun, M., Voit, G. M., Donahue, M., et al. 2009, *ApJ*, 693, 1142
- Sunyaev, R., Arefiev, V., Babyshkin, V., et al. 2021, *A&A*, 656, A132
- Tempel, E., Tuvikene, T., Kipper, R., & Libeskind, N. I. 2017, *A&A*, 602, A100
- Thölkens, S., Lovisari, L., Reiprich, T. H., & Hasenbusch, J. 2016, *A&A*, 592, A37
- Tinker, J., Kravtsov, A. V., Klypin, A., et al. 2008, *ApJ*, 688, 709
- Tornatore, L., Borgani, S., Dolag, K., & Matteucci, F. 2007, *MNRAS*, 382, 1050
- Tornatore, L., Borgani, S., Matteucci, F., Recchi, S., & Tozzi, P. 2004, *MNRAS*, 349, L19
- Vikhlinin, A., Kravtsov, A., Forman, W., et al. 2006, *ApJ*, 640, 691
- Virtanen, P., Gommers, R., Oliphant, T. E., et al. 2020, *Nature Methods*, 17, 261
- Voevodkin, A., Borozdin, K., Heitmann, K., et al. 2010, *ApJ*, 708, 1376
- Voit, G. M., Kay, S. T., & Bryan, G. L. 2005, *MNRAS*, 364, 909
- Weinberger, R., Springel, V., Hernquist, L., et al. 2017, *MNRAS*, 465, 3291
- Wiersma, R. P. C., Schaye, J., & Smith, B. D. 2009a, *MNRAS*, 393, 99
- Wiersma, R. P. C., Schaye, J., Theuns, T., Dalla Vecchia, C., & Tornatore, L. 2009b, *MNRAS*, 399, 574
- Wilms, J., Allen, A., & McCray, R. 2000, *ApJ*, 542, 914
- Yeung, M. C. H., Freyberg, M. J., Ponti, G., et al. 2023, *A&A*, 676, A3
- Zhang, X., X., .., & et al. in prep.
- ZuHone, J., Bahar, Y. E., Biffi, V., et al. 2023, *A&A*, 675, A150

¹⁷ <https://pypi.org/project/pyFFTW/>

¹⁸ <https://heasarc.gsfc.nasa.gov/docs/xanadu/xspec/python/html/>

¹⁹ <https://scipy.org/>

²⁰ <https://pypi.org/project/vorbin/>

Appendix A: Energy band selection for the imaging analysis

We choose the energy band for the imaging analysis by optimizing the signal-to-noise ratio given multiple X-ray foreground and background components. The models we used during this optimization scheme include 1) a 0.1 keV unabsorbed APEC component for the Local Hot Bubble, whose flux is scaled to $2.3 \times 10^{-13} \text{ erg s}^{-1} \text{ cm}^{-2} \text{ deg}^{-2}$ in the 0.3–0.7 keV band (Yeung et al. 2023); 2) a 0.18 keV absorbed APEC component for the Galactic Halo, whose absorbed flux is scaled to $1.1 \times 10^{-12} \text{ erg s}^{-1} \text{ cm}^{-2} \text{ deg}^{-2}$ in the 0.5–2.0 keV band (Henley & Shelton 2013); 3) a $\Gamma = 1.4$ power law component for the Cosmic X-ray Background component, whose absorbed flux is scaled to $6 \times 10^{-13} \text{ erg s}^{-1} \text{ cm}^{-2} \text{ deg}^{-2}$ in the 0.5–2.0 keV band, that corresponds to a $10^{-13} \text{ erg s}^{-1} \text{ cm}^{-2}$ point source flux cut; and 4) the instrumental background from eROSITA filter-wheel-closed observations. The foreground HI column density is fixed to $2.7 \times 10^{20} \text{ cm}^{-2}$ for this study, which is the averaged value of the sample. With these foreground and background configuration, we find that the signal-to-noise ratio of a $T = 1$ keV APEC source component at the redshift of 0.18 reaches the maximum in the 0.3–1.8 keV band at a source-to-background ratio of 1. We note that the upper boundary of the optimal band could increase if we adopt a higher source-to-background ratio since the $\log N - \log S$ curve of the selected sample is a power law. Nevertheless, we select a source-to-background ratio of 1 and we adopt the 0.3–1.8 keV band for our imaging analysis to maintain high signal-to-noise for the faint sources.